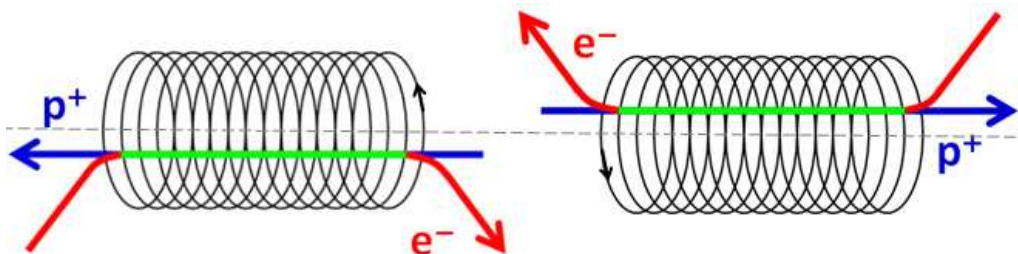


RHIC electron lenses design report

W. Fischer, Y. Luo, and A. Pikin (editors)

E. Beebe, D. Bruno, X. Gu, R.C. Gupta, R. de Maria, A. Fedotov,
D. Gassner, J. Hocke, A. Jain, R. Lambiase, M. Mapes, W. Meng,
C. Montag, B. Oerter, M. Okamura, A. Pikin, D. Raparia,
G. Robert-Demolaize, Y. Tan, R. Than, J. Tuozzolo



October 7, 2010

Contents

1	Introduction <i>W. Fischer, Y. Luo</i>	2
2	Accelerator physics <i>W. Fischer, Y. Luo, C. Montag</i>	3
2.1	Compensation scheme <i>W. Fischer</i>	5
2.2	RHIC lattice modifications <i>C. Montag</i>	6
2.3	Simulations <i>Y. Luo</i>	6
2.4	Luminosity gain <i>Y. Luo, W. Fischer</i>	7
3	Design considerations <i>W. Fischer, Y. Luo, A. Pikin</i>	7
4	Electron gun <i>A. Pikin, J. Hock</i>	9
5	Electron beam transport <i>X. Gu, M. Okamura, D. Raparia, A. Pikin</i>	10
5.1	Transport solenoid design	10
5.2	Steering dipole magnets design	11
5.3	Magnets design specifications	13
6	Main solenoid and insert	13
6.1	Superconducting main solenoid <i>A. Pikin, W. Fischer, J. Hock</i>	13
6.2	Field measurement system <i>A. Jain</i>	13
6.2.1	Mapping of the axial field	14
6.2.2	Measurement of the field straightness	14
6.3	Solenoid field correction system and electron beam steering <i>A. Jain</i>	19
6.3.1	Correctors for solenoid axis straightening	19
6.3.2	Correctors for solenoid axis alignment	21
7	Electron collector <i>A. Pikin, J. Hock</i>	22
8	Power supplies <i>R. Lambiase</i>	23
9	Vacuum system <i>M. Mapes</i>	24
9.1	Gun and collector vacuum	24
9.2	RHIC vacuum interface	25
10	Instrumentation <i>D. Gassner, C. Montag</i>	26
10.1	Electron current modulator	26
10.2	Relative electron-proton beam alignment	27
10.3	Electron beam diagnostics	29
10.4	Proton beam diagnostics	30
11	Infrastructure and installation <i>W. Fischer</i>	30
12	Controls <i>E. Beebe, B. Oerter</i>	31
13	Commissioning and operation <i>W. Fischer, Y. Luo, C. Montag</i>	31
14	Acknowledgements	31

1 Introduction *W. Fischer, Y. Luo*

In polarized proton operation the luminosity of RHIC, like in other colliders, is limited by the beam-beam effect [1–3], and methods that mitigate the effect will result in higher peak and average luminosities. In RHIC stores there are 2 head-on beam-beam interactions at IP6 and IP8, and 4 long-range beam-beam interactions at the other IPs (see Fig. 1). At these other IPs the beams are vertically separated by 10 mm which makes the long-range effect insignificant.

With the head-on beam-beam effect dominating in RHIC we consider the partial indirect compensation of the head-on beam-beam effect with one electron lenses in each of the RHIC rings. Together with intensity and emittance upgrades in RHIC, our goal is to approximately double the luminosity with head-on beam-beam compensation over what can be achieved without it (Tab. 1). A RHIC electron lens consists of (Fig. 2:

- a dc electron gun,
- an electron beam transport system from the gun to the main solenoid,
- the superconducting main solenoid in which the interaction with the hadron beam occurs,
- an electron beam transport system from the main solenoid to the collector, and
- an electron collector.

The 2 electron lenses are located in IR10 between the DX magnets (see Fig. 3). The proton beams pass through the main solenoids of both electron lenses, which have different polarity and therefor locally compensate each other for both linear coupling and spin effects. The electron beam in an electron lens interacts head-on with only one of the proton beams. Table 1 shows the main proton beam parameters for the most recent RHIC Run-9, and with upgrades without and with the electron lenses.

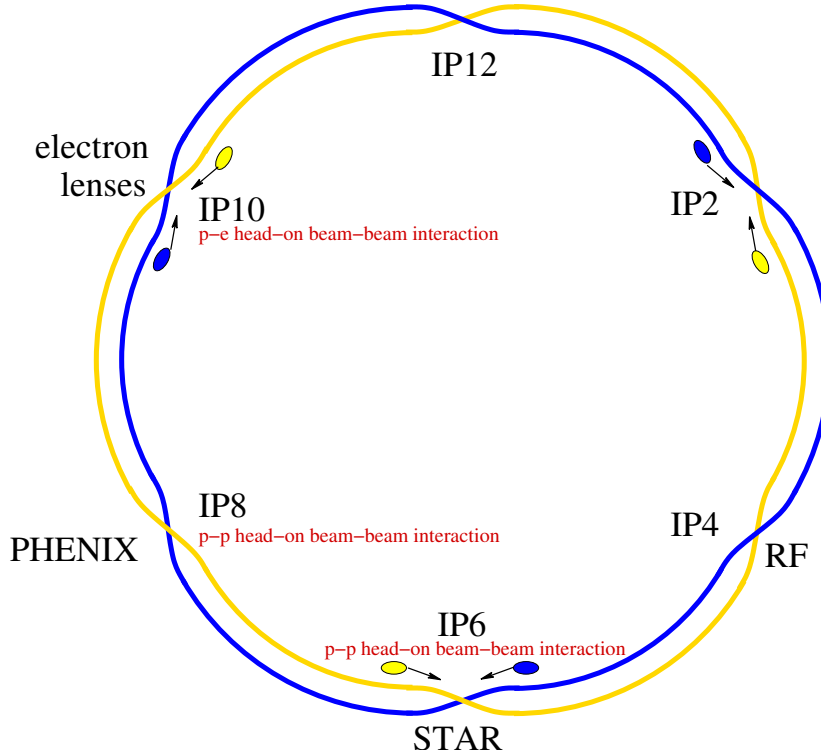


Figure 1: General layout of RHIC with locations of the head-on beam-beam interactions and electron lenses.

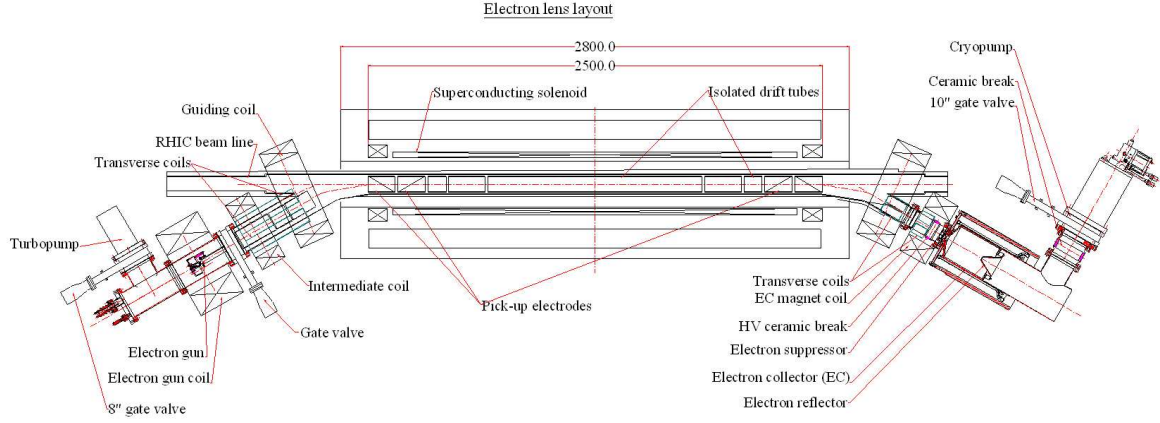


Figure 2: Top view of the electron lens layout with gun, electron transport, main solenoid, electron transport, and collector.

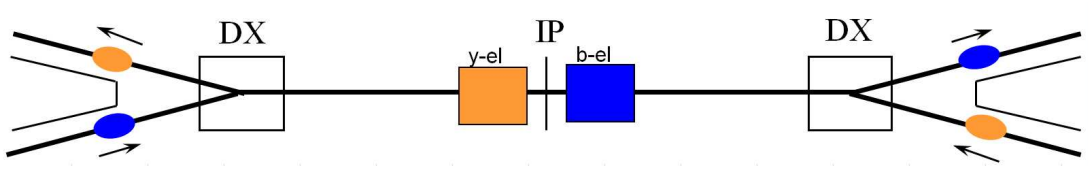


Figure 3: Top view of IR10 with 2 electron lenses located between the DX magnets, a beam pipe section common to both beam.

2 Accelerator physics *W. Fischer, Y. Luo, C. Montag*

Beam-beam effects have limited the performance of previous and existing hadron colliders [4,5,9] such as the Sp̄pS [10–13], Tevatron [14–16] and RHIC [1–3], and are also expected to limit the performance of the LHC [17–25]. Beam-beam effects can be categorized as either incoherent (dynamic aperture and beam lifetime), PACMAN (bunch-to-bunch variations), or coherent (beam oscillations and instabilities) [21]. These effects can be caused by both head-on and long-range interactions. Head-on effects, leading to tune shifts and spreads, are important in all hadron colliders. Total beam-beam induced tune shifts as large as 0.028 were achieved in the Sp̄pS [13] and Tevatron [16], although operational tune shift values are somewhat lower.

Long-range effects, however, differ in previous and existing colliders [26]. In RHIC, where both beams share a pipe only in the interaction regions, there are nominally no long-range beam-beam interactions under store conditions in the interaction regions with collisions. In the interaction regions without head-on collisions there is one long-range interaction each, with a transverse separation of at least 15σ . Long-range interactions have affected the RHIC ramp transmission in the past [1].

Head-on compensations schemes can be divided into three categories [27]:

1. Direct space charge compensation (4 beams)
2. Indirect space charge compensation (electron lenses)
3. Betatron phase cancellation

Table 1: RHIC parameters for beam-beam compensation of polarized protons beams.

quantity	unit	achieved Run-9		goal without electron lenses		goal with electron lenses and other upgrades*	
						case 1	case 2
beam energy E_p	GeV	100	250	100	250	100	250
bunch intensity N_p	10^{11}	1.35	1.1	1.35	1.5	1.8	2.0
no of colliding bunches N	...	107	107	107	107	107	107
average beam current	mA	180	150	180	200	238	270
transverse parameters							
transverse tunes (Q_x, Q_y)	...	(28.695, 29.685)		(28.695, 29.685)		(28.695, 29.685)	
chromaticities (Q'_x, Q'_y)	...	(+2, +2)		(+2, +2)		(+2, +2)	
$\beta_{x,y}^*$ at IP6, IP8 (p-p)	m	0.7	0.7	0.85	0.5	0.85	0.5
$\beta_{x,y}^*$ at IP10 (e-p)	m	7.5	7.5	10.0	10.0	10.0	10.0
rms emittance ϵ_n , initial	mm mrad	2.5	3.0	2.5	2.5	2.5	2.5
rms beam size at IP6, IP8 $\sigma_{x,y}^*$	μm	130	90	110	70	110	70
rms beam size at IP10 $\sigma_{x,y}^*$	μm	420	265	485	310	485	310
longitudinal parameters							
9 MHz rf system, h/V_{gap}	... / MV	—		120 / 0.02		120 / 0.02	
28 MHz rf system, h/V_{gap}	... / MV	360 / 0.3		360 / 0.3		360 / 0.3	
56 MHz rf system, h/V_{gap}	... / MV	—		720 / 2.0		720 / 2.0	
197 MHz rf system, h/V_{gap}	... / MV	—		2520 / 3.5		2520 / 3.5	
rms bunch area S , initial	eV s	0.40	0.30	0.17	0.17	0.17	0.17
rms bunch length σ_s	m	0.85*	0.60*	0.55*	0.25 [†] /0.15 [‡]	0.30 [†] /0.20 [‡]	0.25 [†] /0.15 [‡]
rms momentum spread $\delta p/p$	10^{-3}	0.45*	0.20*	0.30*	0.30 [†] /0.45 [‡]	0.55 [†] /0.85 [‡]	0.30 [†] /0.45 [‡]
no of beam-beam IPs	...	2	2	2	2	(2+1)**	(2+1)**
hourglass factor F , initial	...	0.70	0.80	0.85	0.88 [†]	0.95 [†]	0.88 [†]
beam-beam parameter ξ/IP	...	0.007	0.005	0.007	0.007	0.009	0.010
peak luminosity $\mathcal{L}_{peak}/\text{IP}$	$10^{30}\text{cm}^{-2}\text{s}^{-1}$	50	85	50	250	100	500
average luminosity $\mathcal{L}_{avg}/\text{IP}$	$10^{30}\text{cm}^{-2}\text{s}^{-1}$	28	55	30	150	60	300

*These upgrades are a polarized source upgrade for more bunch intensity and upgrades in RHIC for better polarization transmission to 250 GeV and more total intensity, including improvements to the beam loss control, collimation, and beam dump.

*Longitudinal focusing with 28 MHz rf system.

[†]Longitudinal focusing with 56 MHz rf system.

[‡]Longitudinal focusing with 197 MHz rf system.

**One head-on collision in IP6 and IP8 each, and a compensating head-on collision in IP10.

Betatron phase cancelation refers to the phase adjustment between beam-beam interaction points in order to cancel resonance driving terms. This cannot be done for all resonances, and no successful use in operation has been demonstrated yet.

Direct space charge compensation with 4 beams was proposed for the e^+e^- -colliders COPPELIA [28], DCI [29], and again for B-factories [30]. The only test thus far was done in the 4-beam e^+e^- collider DCI. The DCI experience however fell short of expectation because of strong coherent effects [31–35].

Indirect space charge compensation with an electron lens essentially eliminates the problem of coherent effects since the electron beam in the lens cannot couple back to the proton beam, except for single pass phenomena. Indirect space charge compensation was proposed for CESR [36] the SSC [37, 38], the Tevatron [39], the LHC [40, 41], and RHIC [48].

Two electron lenses are currently installed in the Tevatron [45] where they are reliably used as an operational gap cleaner [46]. They were also shown to improve the lifetime of antiproton bunches suffering from PACMAN effects [47]. The experience with the construction and operation of the Tevatron electron lenses provides invaluable input into an assessment of the practicability of head-on beam-beam compensation.

2.1 Compensation scheme *W. Fischer*

If a collision of a proton beam with another proton beam is followed by a collision with an electron beam, the head-on beam-beam effect can in principle be ameliorated [26].

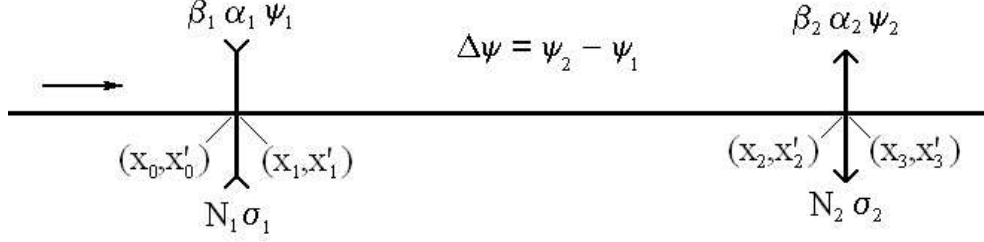


Figure 4: Schematic of head-on beam-beam compensation. At the first location, with lattice parameters $(\beta_1, \alpha_1, \psi_1)$, a proton experiences a beam-beam kick from another proton bunch with intensity N_1 and rms beam size σ_1 . At the second location, with lattice parameters $(\beta_2, \alpha_2, \psi_2)$, another beam-beam kick is generated by the electron beam with effective bunch intensity N_2 and rms beam size σ_2 .

Figure 4 shows the layout of a head-on compensation. For simplicity we only consider the horizontal plane and beams with a Gaussian transverse distribution. Before experiencing a beam-beam kick from another ion beam at location 1, a proton has the transverse phase space coordinates (x_0, x'_0) . Then the proton receives a kick from the other proton beam [43]

$$\Delta x'_0 = \frac{2N_1 r_0}{\gamma x_0} \left[1 - \exp\left(-\frac{x_0^2}{2\sigma_1^2}\right) \right] \quad (1)$$

where N_1 is the bunch intensity of the other proton beam, γ the relativistic factor of the proton receiving the kick, r_0 the classical proton radius, and σ_1 the rms beam size of the other proton beam. The new coordinates are then

$$x_1 = x_0 \quad (2)$$

$$x'_1 = x'_0 + \Delta x'_0. \quad (3)$$

After transport through the linear beam line the coordinates are

$$x_2 = M_{11}x_1 + M_{12}x'_1 \quad (4)$$

$$x'_2 = M_{21}x_1 + M_{22}x'_1 \quad (5)$$

with [44]

$$M_{11} = \sqrt{\frac{\beta_2}{\beta_1}} (\cos \Delta\psi + \alpha_1 \sin \Delta\psi) \quad (6)$$

$$M_{12} = \sqrt{\beta_1 \beta_2} \sin \Delta\psi \quad (7)$$

$$M_{21} = -\frac{1 + \alpha_1 \alpha_2}{\sqrt{\beta_1 \beta_2}} \sin \Delta\psi + \frac{\alpha_1 - \alpha_2}{\sqrt{\beta_1 \beta_2}} \cos \Delta\psi \quad (8)$$

$$M_{22} = \sqrt{\frac{\beta_1}{\beta_2}} (\cos \Delta\psi - \alpha_2 \sin \Delta\psi) \quad (9)$$

and $\Delta\psi = \psi_2 - \psi_1$. In the electron lens the proton receives the kick

$$\Delta x'_2 = -\frac{2N_2 r_0}{\gamma x_2} \left[1 - \exp\left(-\frac{x_2^2}{2\sigma_2^2}\right) \right] \quad (10)$$

where N_2 is the effective bunch intensity of the electron lens beam (i.e. the number of electrons the proton passes in the lens), and σ_2 the rms beam size of the electron lens beam. The coordinates after passing the electron lens are then

$$x_3 = x_2 \quad (11)$$

$$x'_3 = x'_2 + \Delta x'_2. \quad (12)$$

One can now express the final coordinates (x_3, x'_3) as a function of the intensities (N_1, N_2) and require for exact compensation that

$$x_3(N_1, N_2) = x_3(0, 0) \quad \text{and} \quad (13)$$

$$x'_3(N_1, N_2) = x'_3(0, 0), \quad (14)$$

i.e. the final coordinates are the same with and without beam-beam interaction and compensation. From the condition (13) it follows that $M_{12} = 0$ and therefore $\Delta\psi = k \cdot \pi$, with k being an integer. From the condition (14) it follows that $N_1 = N_2$ and $\sigma_1^2/\sigma_2^2 = \beta_1/\beta_2$. Therefore, if the following three conditions are met the beam-beam kicks are canceled exactly:

1. There are no nonlinearities between the two collisions.
2. The phase advance between the p-p and p-e collisions is a multiple of π in both transverse planes.
3. The proton and the electron beam produce the same amplitude dependent forces by having the same effective charge, transverse and longitudinal profile.

In practice this cannot be achieved exactly, but if these conditions are met sufficiently close we expect an increase in the luminosity large enough to make head-on beam-beam compensation worthwhile.

2.2 RHIC lattice modifications *C. Montag*

As part of the electron lens installations, several modifications to the RHIC lattice are necessary. To relax the alignment tolerances between the circulating proton beam and the electron lens beam as well as the straightness requirements on the electron lens solenoid, the transverse rms beam size of the proton beam should be maximized. Using the latest 250 GeV polarized proton lattice, the leads and power supplies in IR10 allow for a maximum β -function of $\beta^* = 10$ m at the interaction point. For a 250 GeV proton beam with a normalized rms emittance of $\epsilon_n = 2.5$ mm mrad this translates into a transverse rms beam size of $\sigma = 310 \mu\text{m}$.

As shown in the previous subsection, head-on beam-beam compensation requires a betatron phase advance of $k \cdot \pi$ between the proton-proton interaction point and the electron lens, where k is an integer. To adjust the betatron phase advance between IPs 8 and 10 in RHIC, additional shunt supplies will be installed on the main quadrupoles in the arc between these two IPs.

2.3 Simulations *Y. Luo*

RHIC simulations Refs. [50–56], general simulation Ref. [57], need other from Tevatron/LHC.

- short-term, single particle (footprint, tune diffusion, Lyapunov)

- long-term, single particle (benchmarking with RHIC data, beam lifetime, emittance growth)
- long-term diffusion (N. Abreu's work)
- long-term, multi-particle (J. Qiang, Y. Luo)

2.4 Luminosity gain *Y. Luo, W. Fischer*

The luminosity gain can be estimated in two ways. First, an estimate can be derived from RHIC beam lifetime observations, assuming that the effective beam-beam parameter can be reduced by a certain amount. Second, an estimate can be derived from simulations.

Estimate based on lifetime observations (W. Fischer).

Without increase in bunch intensity

With increase in bunch intensity Increase by 50%, keep total current constant ...

- 250 GeV: retain old projections
- 100 GeV: reached beam-beam limit in Run-9, expect somewhat smaller final beam-beam parameter with electron lens

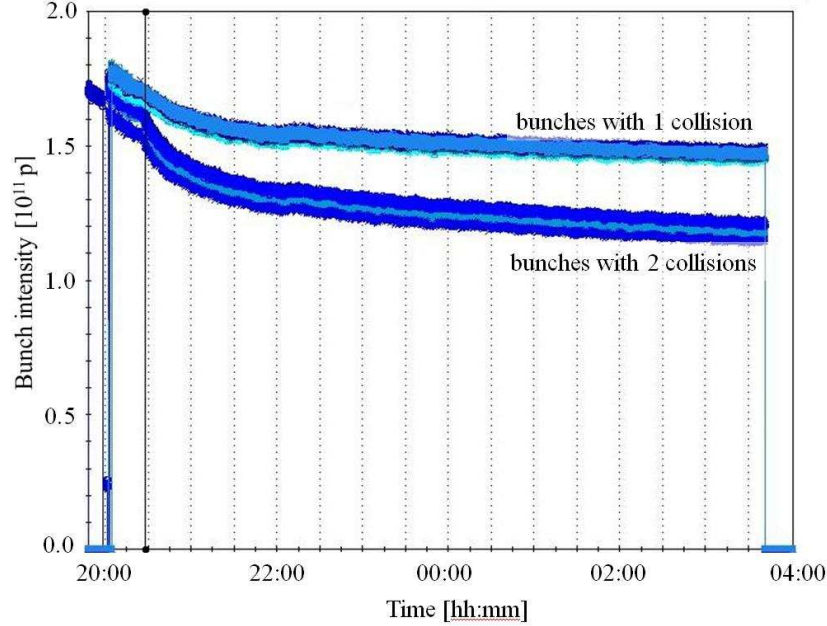


Figure 5: Run-8, fillno 9989

Estimated based on simulations (Y. Luo).

- compare beam lifetimes with and without head-on beam-beam compensation

3 Design considerations *W. Fischer, Y. Luo, A. Pikin*

In designing the electron lens we are aiming for a technically feasible and economically viable implementation that comes as close as possible to the ideal compensation scheme outlined in Sec. 2.1. In addition,

a major design consideration is the ease of commissioning and operation. Our goal is a commissioning largely parasitic to the RHIC operation for physics. The main design process can be summarized as follows:

Condition 1 in Sec. 2.1 (no nonlinearities between the p-p and p-e interactions) is best realized when the p-e interaction is as close as possible to the p-p interaction. With the location in IR10 (Fig. 1) there is only one arc between the p-p interaction at IP8 and the p-e interaction in IR10. In this configuration, a proton, after receiving a beam-beam kick in IP8, passes a triplet with nonlinear magnetic fields from field errors, an arc with chromaticity sextupoles and dodecapoles in the quadrupoles as dominating nonlinear field errors, and another triplet in IR10. The dodecapole error in the arc quadrupole increase from 6 units (at 25 mm reference radius) to 9 units when the main arc current is increased from 5.0 kA to 5.5 kA [6]. An increase in the main quadrupole current may be considered to change the phase advance between IP8 and IP10 (see below).

Condition 2 in Sec. 2.1 (phase advance of multiples of π between p-p and p-e interaction) can be realized with a phase shifter (see Sec. 2.2).

Condition 3 in Sec. 2.1 (same amplituded dependent forces from proton beam and electron lens) has a number of implications. Since both beam proton beams are round in the beam-beam interactions ($\beta_x^* = \beta_y^*$ and $\epsilon_x = \epsilon_y = \epsilon_n$), we also require $\beta_x = \beta_y$ and matched transverse proton and electron beam profiles, i.e. the electron beam profile is also Gaussian with $\sigma_{p,x} = \sigma_{e,x} = \sigma$ and $\sigma_{p,y} = \sigma_{e,y} = \sigma$. $\beta_x = \beta_y$ limits the electron lens locations to the space between the DX magnets. In these locations the RHIC lattice also has a small dispersion.

The tolerances for the main solenoid field straightness, and the tolerances for the relative beam alignment are easier to meet with a larger proton beam. The β -function at IP10 cannot be larger than 10 m at 250 GeV proton energy without modifications to the IR10 triplets. Such modifications are currently not considered because of costs.

The electron beam size in the main solenoid σ_e is given by its size at the cathode σ_{ec} , and the solenoid fields at the cathodes and in the main solenoid as $\sigma_e = \sigma_{ec} \sqrt{B_{sc}/B_{sm}}$. The field B_{sm} cannot be much larger than 6 T, and a strong field makes a correction of the field straightness more difficult. The field B_{sc} has to be large enough to suppress unwanted space charge effects. With the limits in the B_{sc} and B_{sm} fields, and a given beam size σ_e the electron beam size and current density at the cathode follow, and must be technically feasible. Unlike the Tevatron electron lenses we use a DC electron beam to avoid the noise possibly introduced through the high voltage switches.

The location of both the Blue and Yellow electron lens in IR10, in a section common to both beams (Fig. 1), allows the local compensation of the main solenoid effect on both linear coupling and spin orientation by having the two main solenoids with opposing field orientation. In this configuration it is also possible to ramp the magnets together during RHIC stores without affecting the beam lifetime or spin orientation.

The instrumentation must allow monitoring the electron beam current and shape as well as the relative position and angle of the electron and proton beam in the electron lens. Two modes are foreseen: a setup mode in which the electron beam current is modulated, and a compensation mode with a DC electron beam. The main parameters of the electron lens sub-systems are presented in Tab. 2.

Table 2: RHIC electron lens parameters. Case 1 and case 2 are the same as in Tab. 1 and refer to the electron lens upgrade for 100 GeV and 250 GeV proton beam energy respectively. Case 3 is also for 250 GeV but with a proton bunch intensity increased by 50%.

parameter	unit	case 1	case 2	case 3
proton beam				
beam energy E_p	GeV	100	250	250
relativistic γ_p	...	107	266	266
bunch intensity N_p	10^{11}	1.8	2.0	3.0
transverse rms emittance ϵ_n	mm mrad	2.5	2.5	2.5
$\beta_{x,y}$ at e-lens location	m	10	10	10
rms beam size at e-lens location	μm	485	310	310
no of beam-beam IPs	...	2	2	2
beam-beam compensation degree	%	50	50	50
electron gun				
cathode material	...	— IrCe —		
transverse beam profile	...	— Gaussian —		
cathode radius r_c	mm	— 3.5 —		
rms beam size at cathode r_{ec}	mm	— 1.7 —		
perveance	$\mu\text{A V}^{-3/2}$	— 1.23 —		
solenoid field B_{sc}	T	0.49	0.20	0.20
voltage	kV	5.8	6.4	9.2
beam relativistic β_e	...	0.15	0.16	0.19
electron current I_e	A	0.5	0.6	1.1
max. current density	A cm^{-2}	3.0	3.4	6.0
cathode lifetime	h	— more than 30,000 —		
electron beam power	kW	3.1	4.0	10.1
static pressure	Torr			
dynamic pressure	Torr			
electron transport, gun to main solenoid				
...				
main solenoid section				
beam pipe radius R	mm	— 40.0 —		
electron rms beam size σ_e	μm	485	310	310
perveance of beam pipe	$\mu\text{A V}^{-3/2}$	2.6	2.4	2.4
solenoid length	m	— 2.5 —		
length of good field quality L	m	— 2.1 —		
solenoid field strength B_{sm}	T	— 6.0 —		
no of electrons seen by protons	10^{11}	1.8	2.0	3.0
no of electrons in lens	10^{11}	1.6	1.7	2.5
integrated current ($I_e L$)	A m	1.1	1.3	2.3
electron transport, main solenoid to collector				
same parameters as gun to main solenoid transport				
electron collector				
surface material	...	— Cu —		
power deposited	kW	3.1	4.0	10.1
average power density	W cm^{-2}			
maximum power density	W cm^{-2}			
maximum temperature increase	K			
static pressure	Torr			
dynamic pressure	Torr			

4 Electron gun *A. Pikin, J. Hock*

The electron gun for the electron lens has to provide a beam with a radial distribution of the emission current density close to a Gaussian to match the radial charge density distribution in the stored proton beam. The proton beam in interaction region has an rms beam size of 310 μm (Tab. 2). To have a close to Gaussian profile, one goal in the electron gun design is to have a ratio of electron beam radius to its rms beam size of approximately 3. Considering only magnetic compression of the electron beam into

center of solenoid with maximum magnetic field of 6.0 T the choice of cathode diameter of 7.0 mm gives a comfortable margin of magnetic fields on the cathode and in the center of superconducting solenoid. The requirement to have a Gaussian distribution of current density was met by using an electron gun immersed in a magnetic field. This gun has a control electrode between the cathode and the anode similar to the Fermilab gun design [45], and a shaped cathode surface to suppress emission in areas where the control electrode leaves the electric field not sufficiently low. The simulation of the electron gun and electron collector has been done with 2D package Tricomp from Field Precision [7]. The electrostatic model of simulations is presented in Fig. 6.

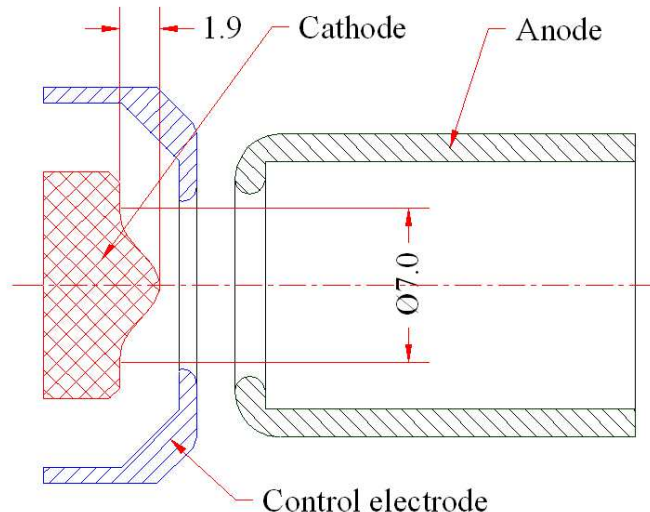


Figure 6: Electrostatic model of the electron gun.

The simulated emission profiles are presented in Fig. 7 for 3 values of the control electrode voltage. The electron current is $I_{el} = 1.06$ A, and an anode voltage $U_{an} = 11.5$ kV. The perveance of this gun is $P_{gun} = 0.86 \times 10^{-6} \text{ AV}^{-1.5}$. The radial emission current density has the shape of Gaussian curve for voltage on control electrode $U_{CE} = -311.0$ V. For these parameters of the gun the Gaussian fit has the parameters $\sigma_{emission} = 1.24$ mm and $\alpha_{emission} = 20.92 \text{ A cm}^{-2}$. The ratio of cathode radius to the rms of the Gaussian fit is $r_{cath}/\sigma_{emission} = 2.82$. One can see that the current density of the electron beam on its radial periphery can be changed with the control electrode voltage while the general shape of the beam profile remains Gaussian.

For this the electron gun the cathode should be capable of providing an emission current densit of about 21 A cm^{-2} for an electron beam current of 1 A continuously and in a regime of short pulses with a reasonable life time of several thousand hours. Cathodes made of IrCe [8] satisfy these requirements.

The simulated electron trajectories in the vicinity of the cathode are presented in Fig. 8 for a magnetic field on the cathode of $B_c = 0.4$ T.

5 Electron beam transport *X. Gu, M. Okamura, D. Raparia, A. Pikin*

5.1 Transport solenoid design

To design electron lens beam transport system, the most important thing is to transport electron beam from gun side to collector side, control electron beam trajectories to follow the center line of superconducting main magnet (SM).

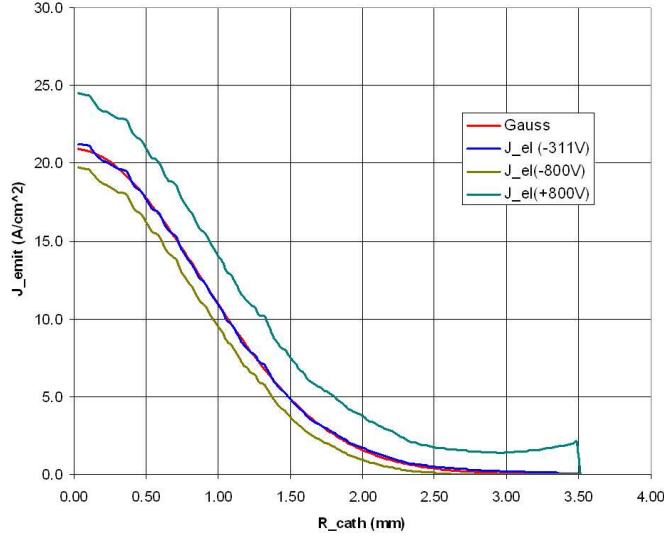


Figure 7: Radial distributions of the emission current density for $I_{el} = 1.06$ A, $U_{an} = 11.5$ kV and different voltages on the control electrode. The red line is a Gaussian fit.

Because gun side and collector side have almost identical solenoid design, six warm magnets are placed symmetrically around SM. Figure 9 is the layout of one electron lens, which has gun side, SM and collector side. Each side of one electron lens has three magnets; they are GS1, GS2 and GSB on left side, and CS1, CS2 and CSB on right side.

With electron lens default operation configuration, electron beam comes out from electron gun firstly, and then goes through GS1, GS2 and GSB. After that, it starts to enter the SM magnet, passes SM along the center line of this magnet. Then, it is transported from CSB, CS2 and CS1. Finally, it is dumped into a collector. This procedure is also shown as the green line in Fig. 9, which starts from gun side to collector side.

According our design considerations in Sec. 3, the electron beam size should match the proton beam size inside SM. That means beam transport system should also have capability to change the magnetic field ratio between SM and GS1. GS1 can change its field from 0.2 T to 0.8 T and magnetic field of SM can change from 1 T to 6 T, this will change almost 5 times beam size from its minimum value $\sigma_{gun} \sqrt{1/30}$ to its maximum value $\sigma_{gun} \sqrt{4/5}$. And when changing GS1 field or changing beam size, GS1 field will not affect electron beam trajectories.

Electron transport system also should have the magnetic field that large enough to suppress unwanted space charge effects, and should be rigid enough that electron beam can't be disturbed by or disturb other electromagnetic field. The magnetic field along beam trajectories should be greater than 0.3 T. The magnetic field along the center line (the green line in Fig. 9) was plot in Fig. 10). Fig. 11 is the magnetic field map distribution around gun side, which shows the area that the amplitude of magnetic field is greater than 0.3 T.

5.2 Steering dipole magnets design

For electron lens, electron beam should head on collide with proton beam at IP 6 or IP 8. So, it is very important to align electron beam with proton beam. For this purpose, to control electron is easier than to control proton. Because two proton beams share one beam pipe at IP 10 with 10 mm distance between

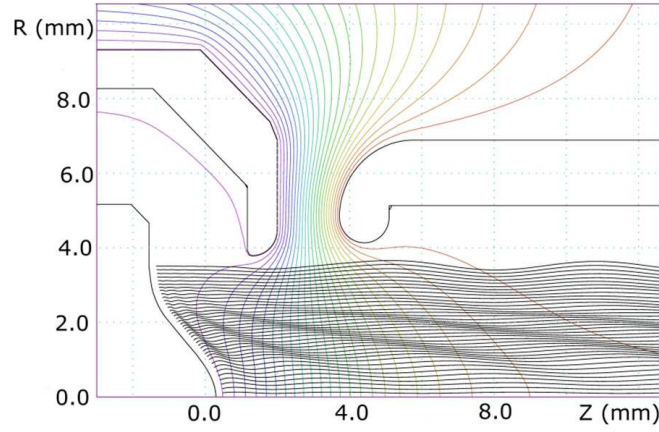


Figure 8: Simulated electron trajectories in a gun with $I_{el} = 1.06$ A, $U_{an} = 11.5$ kV, $U_{CE} = -311$ V, $B_c = 0.4$ T.

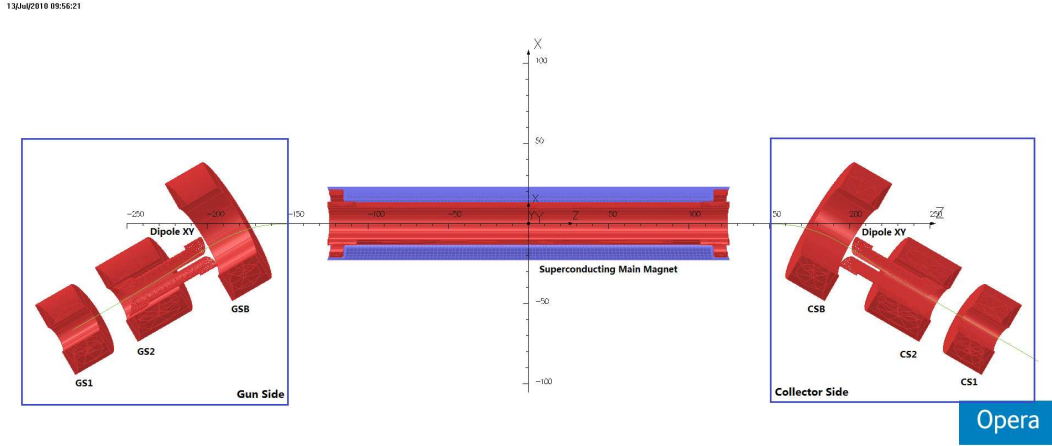


Figure 9: Layout of electron lens.

then, the electron beam should have the capability to shift 5 mm around the center line in horizontal and vertical plane. To satisfy this requirement, two dipole magnets (Dipole X and Dipole Y) are designed for each side of two lenses, and are placed inside of GS2 and CS2.

Fig. 12 is the beam trajectories envelope after using dipole magnet with the center beam trajectory 5 mm shift. In Fig. 4, when the upper line was plot, the electron comes from upper side of cathode and beam was shifted up 5mm. The lower line was plot with the electron produced by lower side of cathode and with beam 5 mm shift down.

According to Fig. 12, we can optimize the tube inner diameter so that the electron beam will not touch its inner side. Tube inner size should also be careful design by technician at last.

Fig. 13 is the geometry of one dipole X, and its magnetic field distribution. Dipole Y has almost same geometry and field distribution like dipole X.

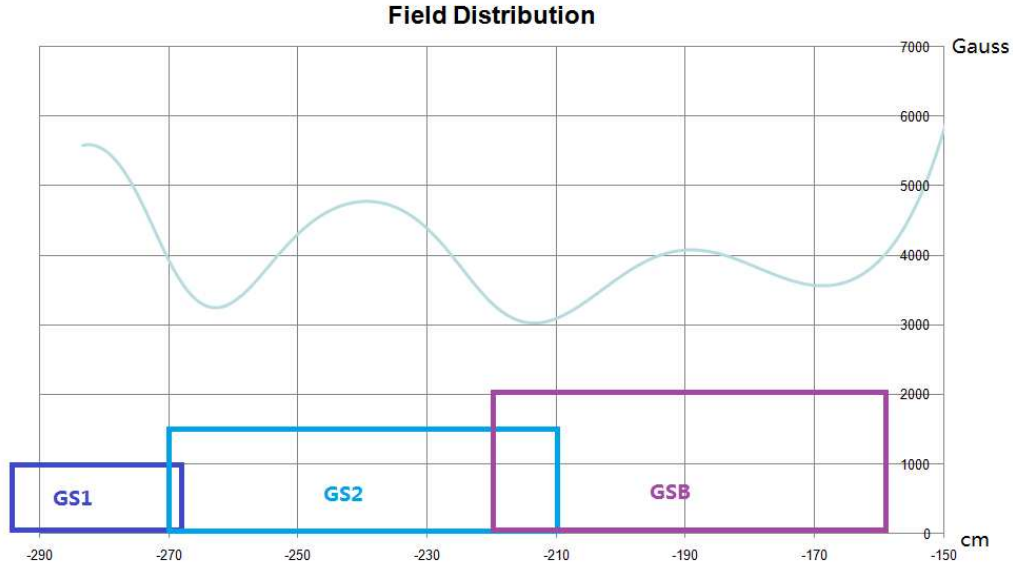


Figure 10: Magnetic field distribution along center trajectory line.

5.3 Magnets design specifications

During electron lens design period, running cost also should be taken for considerations. How to reduce the power consumed in transport system is another important thing. The power consumption for both electron lenses should be limited to 500 kW in order to avoid upgrades to the electrical and water cooling system in IR10.

Figure 14 is our electron lens beam transport system design specifications, including power consumption calculations. The first part in this table includes the position and angle of GS1, GS2 and GSB. The second part of this table is the conductor parameters and the geometry of these magnets. The third part that listed in this table is the power consumption, temperature increase and magnetic field which are caused by these solenoids, and they are given with two different cases, normal optimization case and normal plus 40% current case.

6 Main solenoid and insert

- superconducting main solenoid with warm bore
- warm insert with field straightness correction, and large angle corrector
- drift tubes for ion extraction and instrumentation

6.1 Superconducting main solenoid *A. Pikin, W. Fischer, J. Hock*

6.2 Field measurement system *A. Jain*

The field measurement system for the electron lens solenoid should be capable of measuring the field quality to ensure that the specifications are met for the as-built solenoid, as well as after axis corrections using the correction system. There are two types of measurement systems that are required – (a) for

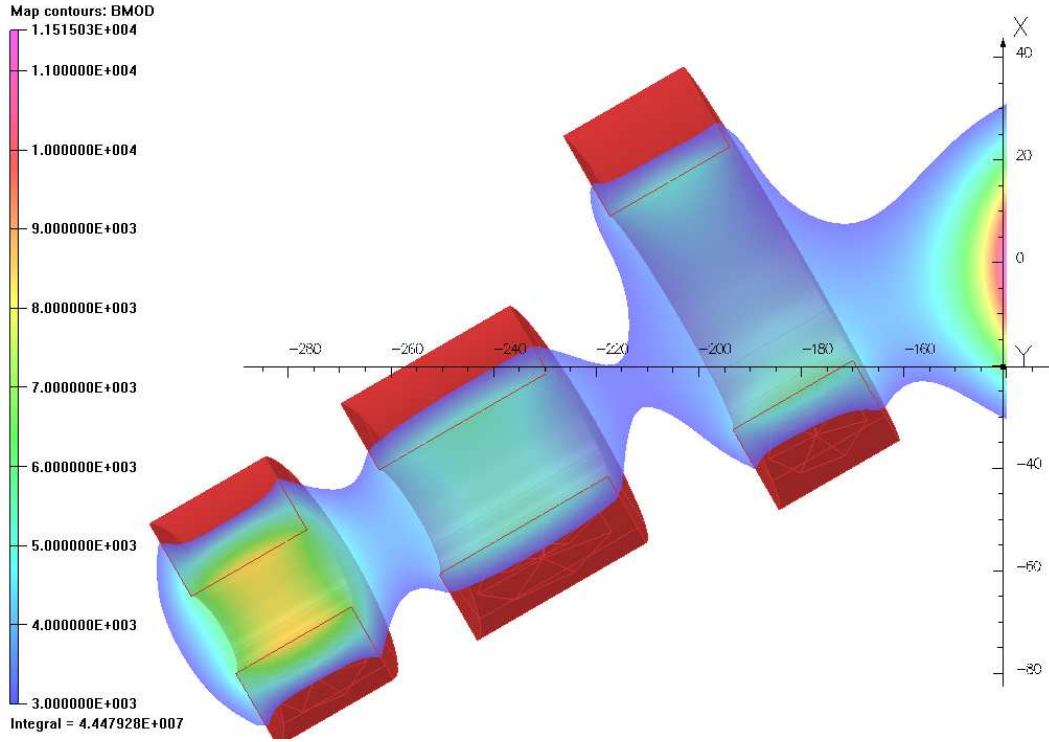


Figure 11: Magnetic field distribution around gun side.

mapping the axial component of the field in a region close to the axis and (b) to measure the straightness of the magnetic field lines.

6.2.1 Mapping of the axial field

The uniformity of axial field in the central ± 1 m region of the solenoid is specified to be better than $\pm 0.5\%$. A Hall probe system will be used for these measurements. The most accurate commercially available Hall probe systems [59] can provide a measurement accuracy as high as $\pm 0.01\%$, but are limited to fields up to 3 T. There are other commercially available Hall probes that can measure very high fields, and some of them may have adequate resolution to measure field uniformity in the $\pm 0.5\%$ range. One such probe could be the 10 T probe from Senis [60], which is expected to have a resolution of about 0.1% at 6 Tesla, or a customized version of the Group 3 probes. Since manufacturers do not provide calibration data beyond 3 T, the probes will have to be calibrated in-house for fields up to 6 T. A Hall probe assembly consisting of one or more probes will be moved along the solenoid axis to measure the on-axis and off-axis field profiles. The position of the Hall probe will be monitored using either a laser interferometer or a precision linear encoder.

6.2.2 Measurement of the field straightness

The field lines in the as-built solenoid are specified to be straight within ± 0.4 mm in the central ± 1 m region. The straightness after corrections should be within 0.025 mm. The field measurement system for this purpose should therefore be capable of resolving axis variations well below 0.025 mm. For a 6 T solenoidal field, and assuming the longest wavelength to be equal to the 5 m length of the solenoid, this

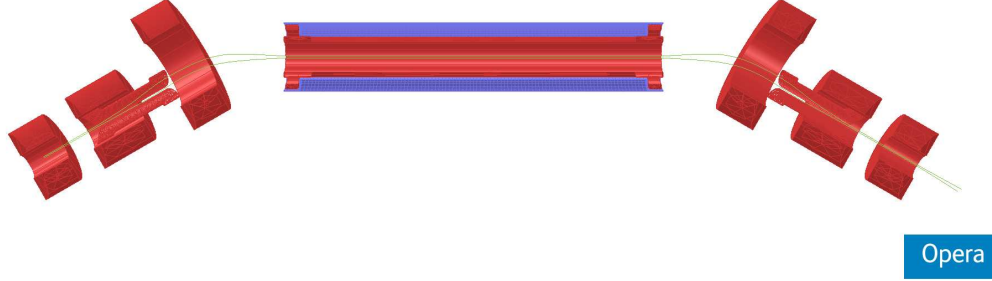


Figure 12: Horizontal Beam Trajectory Envelope with 5mm Shift Up and Down.

amounts to a field angle of about 0.030 mrad, or a local transverse field of roughly 0.2 mT. The field measurement system should therefore have a resolution of at least an order of magnitude smaller than these values (i.e. 0.003 mrad, or 0.02 mT). Since the same system should also be useable to measure the as-built solenoid, the measurement system used should also have a large measurement range up to at least 1 mrad.

Field straightness measurements in solenoids have been carried out in the past using a magnetic needle and mirror system [61]. The use of such a system with μrad range resolution is non-trivial due to many possible error sources [62], thus requiring a significant R&D effort. In view of the limited time available, it is planned to develop a different measurement method based on the vibrating wire technique, first developed at Cornell [63] for measuring quadrupoles and recently adapted and improved at BNL [64] for alignment of multipoles on a girder for the NSLS-II project. The basic principles of this technique, as applied to solenoid measurements, are described below.

Basics of the Vibrating Wire Technique

The basic setup for vibrating wire measurements is shown in Fig. 17. A Cu-Be wire of 0.125 mm diameter is passed through the bore of the solenoid and is supported on both ends by V-notches. One end of the wire is held fixed, while the other end is attached to a weight to keep the wire under the maximum tension possible to minimize sag. A small AC current (< 100 mA) is passed through the wire. If the solenoid axis is perfectly straight, and the wire is perfectly aligned with the solenoid axis, then the wire sees no transverse fields, and there is no force on the wire. If the wire is not aligned with the solenoid axis, or if the solenoid axis is not perfectly straight, the wire sees transverse fields, and thus a periodic force, which causes the wire to vibrate. Any fields in the vertical (Y) direction cause the wire to vibrate along the X-axis, and vice versa. These vibrations are then detected by a pair of wire vibration sensors located at a fixed axial position near one end of the wire, which give an indication of the transverse field components along both X and Y axes. If the frequency of the AC current is chosen to match one of the resonant vibration modes of the wire, then even very small fields can cause easily detectable vibration signals, making this technique extremely sensitive. It has been shown [63] that sensitivities at the 0.02 mT level, needed for measuring even the fully compensated solenoid for the electron lens project, can be readily achieved with this technique.

The relative amplitudes of various vibration modes depend on the axial distribution of the transverse field. For example, the wire vibration in all the even modes must be antisymmetric about the axial center. Such modes are therefore excited by only the axially antisymmetric components of the transverse

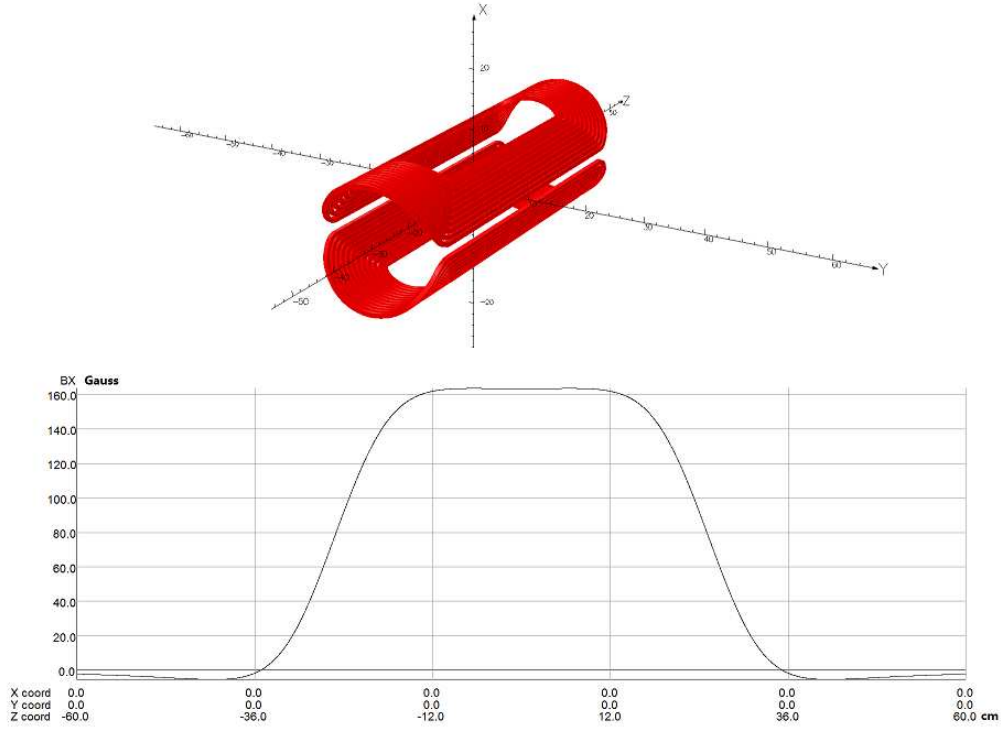


Figure 13: Dipole X and its Magnetic Field Distribution.

field distribution. Similarly, all the odd modes are excited by the axially symmetric components. By measuring the vibration amplitudes for a large number of odd and even modes, one can reconstruct the complete axial profile of the transverse fields. The axial resolution of this profiling depends on the highest vibration mode measured. It is estimated that at least 20 resonant modes can be measured using a 0.125 mm diameter Cu-Be wire. Assuming a wire length of 4.5 to 5 m, an axial resolution of 20-25 cm, or better, can be achieved. This resolution should be sufficient since it is comparable to the diameter of the solenoid aperture, and axis variations at length scales shorter than this are not expected.

Aligning the wire to the solenoid axis – removing tilt

The wire must first be aligned to the solenoid axis so that it does not experience any transverse force along its length due to misalignment. If the wire is tilted with respect to the solenoid axis (but has no offset), it sees nearly a constant transverse field in the central region and the same transverse field on both ends, which depends on the amount of tilt. In other words, the axial distribution of field is symmetric and thus excites only the odd modes. As an illustration, Fig. 18 shows the computed mode amplitudes as a function of tilt in a 2 m long solenoid. One can thus determine the tilt of the wire necessary to align it with the solenoid axis by measuring amplitudes of an odd mode (the fundamental mode, say) as a function of wire tilt.

Aligning the wire to the solenoid axis – removing offset

The tilt adjustment described above makes the wire parallel to the solenoid axis. In addition, the wire offset from the solenoid axis should also be made zero so that it does not experience any transverse forces due to off-axis radial field in the ends. If the wire is offset with respect to the solenoid axis (but has no

E-lens Beam Transport System Design Specification						
		GS1	GS2	GSB	GSX	GSY
		Position and Angle				
Global Position	L_*_GCS (mm)	-1690	-1690	-1850	-1690	-1690
Local Position	L_*_LCS (mm)	1320	820	100	660	660
Angle	Theta (degree)	30	30	30	30	30
		Solenoid Parameters				
Conductor	h_cond (mm)	14	14	14	6.35	6.35
	ID_water(mm)	9	9	9	4.75	4.75
	b_insul (mm)	0.3	0.3	0.3	0.65	0.65
Size	ID(mm)	173.5	234	480	194	210
	OD(mm)	553.1	526	859.6	208	224
	Length(mm)	262.8	379.6	262.8	500	500
	N_Layer	13	10	13	12	12
	N_pan	9	13	9		
	Inductance (Henry)	0.02	0.02	0.04		
	Resistance (ohm)	0.04	0.05	0.08	0.02	0.02
		Optimization				
Power	Power (kW)	58.3	25.6	45	1.4	1.7
	Current(A)	1188	731	769	258	271
Water	Temp_Delta (°C)	13.4	3.6	14.2	5.9	6.9
	Pressure_Drop(Bar)	1.5	1.5	1.5	1.5	1.5
Field	(Gauss)	8000	4468	3202	-	-

Figure 14: Beam transport design parameters.

tilt), it sees practically no transverse field in the central region and equal and opposite transverse fields on the two ends of the solenoid, whose magnitude depends on the amount of offset. In other words, the axial distribution of field is antisymmetric and thus excites only the even modes. As an illustration, Fig. 19 shows the computed mode amplitudes as a function of offset in a 2 m long solenoid. One can thus determine the offset of the wire necessary to align it with the solenoid axis by measuring amplitudes of an even mode (the second harmonic mode, say) as a function of wire offset.

Measuring the axial distribution of transverse field

After the wire is aligned to the solenoid axis using the procedure described above, any residual force seen by the wire must be caused by non-straightness of the solenoid axis. If the solenoid axis is perfectly straight, making any one even mode zero by adjusting the offset of the wire automatically makes all the other modes also zero, as can be seen from Fig. 19. Similarly, if the tilt is adjusted to make any one odd mode zero, all the other odd modes also vanish. There will be no residual force on the wire in this case. However, if the axis of the solenoid is not perfectly straight, the axial distribution of the transverse force is more complex, and all the even (or odd) modes will not vanish for the same wire offset (or tilt). One should choose the lowest order modes with the longest wavelengths (fundamental frequency f_0 , and second order mode $2f_0$) to achieve the “best overall” alignment of the wire to the solenoid axis. In general, all the other odd and even modes will not be zero with this alignment due to non-straightness of the solenoid axis. Measurement of all the remaining vibration mode amplitudes at this point will give

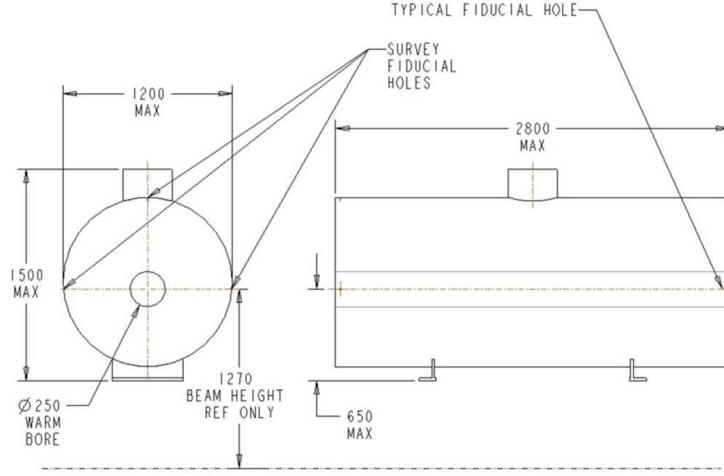


Figure 15: Mechanical dimensions of the main solenoid.

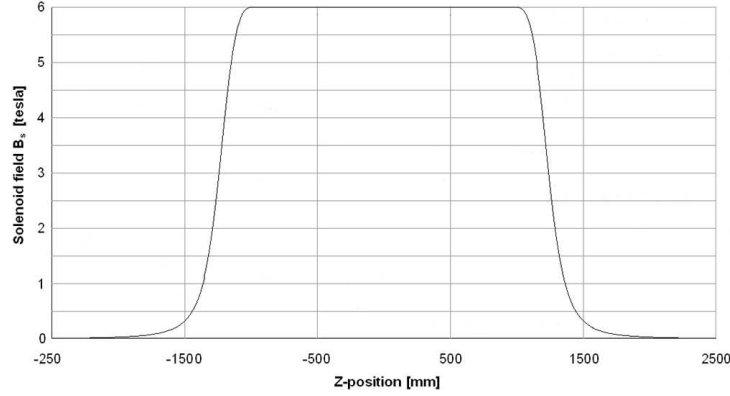


Figure 16: Solenoid field.

the transverse field profile, from which the variation of the solenoid axis as a function of axial position can be derived.

Measurement issues to be addressed

The above description of the solenoid axis measurement scheme assumed a perfect solenoid field and zero wire sag. In practice, the solenoid field will not be perfect and the wire will have appreciable sag, which complicates the analysis. For example, a 5 m long wire (necessary to ensure that the field is practically zero at the wire ends) will sag by about 0.3 mm even with a tension close to the yield limit of the wire. This causes the wire to see transverse fields along its length due to a finite slope with respect to the solenoid axis, as well as a varying vertical offset. These fields are quite significant in comparison to the true fields from axis variations that are to be measured. Therefore, corrections must be applied accurately for the finite wire sag. The amount of wire sag itself can be accurately estimated from the fundamental resonant frequency, which is measured precisely as part of the vibrating wire measurements. Since the wire profile is known accurately, and the solenoid axial field profile can be measured, one can, in principle, compute the contributions from wire sag to various mode amplitudes and correct the measured data for the effect

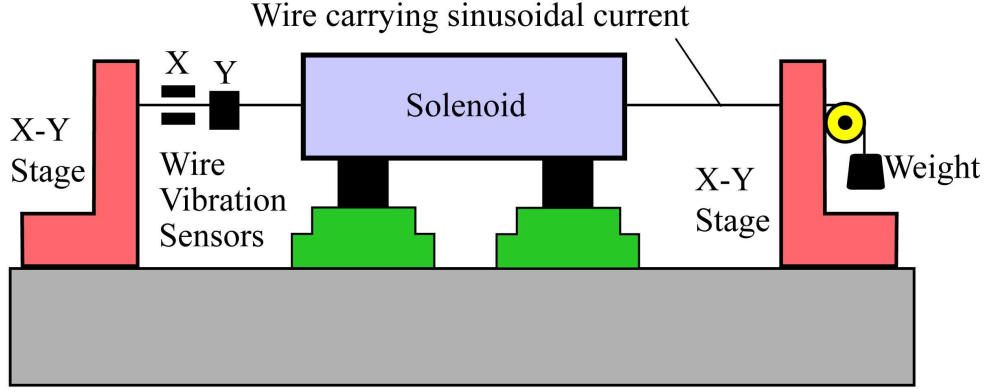


Figure 17: Basic setup for vibrating wire measurements of a solenoid.

of the wire sag. Simulations with a model solenoid with axis straightness errors of about ± 0.25 mm have shown that such a correction can work, at least in theory. However, such a procedure has never been carried out before in practice, and the viability of using the vibrating wire technique needs to be studied further.

In order to address these measurement issues, a prototype measurement system has been built and set up to measure a very low field (< 10 mT), 1.9 m long room temperature solenoid. This system is shown in Fig. 20.

6.3 Solenoid field correction system and electron beam steering *A. Jain*

The straightness of the field lines in the central ± 1 m region of the solenoid is specified to be ± 0.025 mm for optimal performance. It is unlikely that this level of straightness will be achieved in the as-built solenoid. In fact, in order to keep the construction costs and manufacturability realistic, the specification for straightness of the as-built solenoid was only ± 0.2 mm, which is now further relaxed by a factor of 2 based on feedback from the industry. A correction system will therefore be necessary to achieve the final field straightness goals. Such a correction system will consist of a series of short dipole correctors for each of the two transverse axes. In addition, it is planned to have a set of full length correctors to correct any angular misalignment between the overall solenoid field axis and the electron beam. A cross section showing schematically various correctors in the solenoid aperture is given in Fig. 21.

6.3.1 Correctors for solenoid axis straightening

Any deviation of the solenoid axis from a straight line produces a local transverse field whose strength depends on the solenoidal field strength and the local angle of the solenoid axis. The field lines can be straightened if an equal and opposite dipole field is produced by the correctors. For effective correction, the strengths as well as the pitch of these correctors must match the nature of axis variations.

Assuming a sinusoidal variation of the transverse position of the solenoid axis, a , with a wavelength of λ and amplitude a_0 in a solenoidal field of B_0 , the amplitude of transverse field variations is given by

$$B_{\perp} = \left(\frac{2\pi}{\lambda} a_0 B_0 \right). \quad (15)$$

The correction strength needed thus depends on the amplitude of solenoid axis variations, as well as the shortest wavelength expected for this variation. Assuming a shortest wavelength of 1 m (a few times

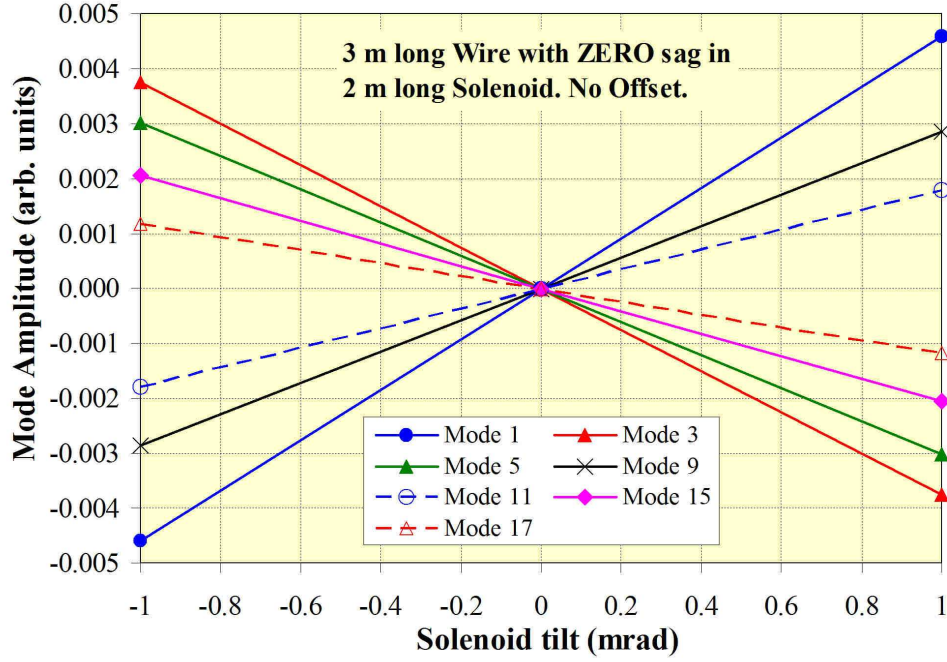


Figure 18: Amplitudes of odd modes as a function of tilt. The even modes are independent of tilt.

the solenoid aperture), and 0.4 mm amplitude (equal to the relaxed specification), the transverse field needed is 15 mT. With a small margin, it should be sufficient to have correctors that can provide about 20 mT dipole field. The number of correctors needed depends again on the shortest wavelength expected. In order to keep the number of power supplies to a bare minimum, as well as to keep a decent length to diameter ratio for the correctors, it is currently planned to have five short correctors per axis, each 0.5 m long, to cover the entire solenoid length of 2.5 m. It should be noted that a given corrector strength can correct larger (or smaller) axis deviations, if the shortest wavelength happens to be longer (or shorter) than that assumed for the design.

As can be seen from Fig. 21, after allowing for the space needed for the beam pipe and the system for bakeout, the radial space available for the correctors is very limited. This calls for the maximum efficiency in the design of these correctors in order to produce the required field with the least amount of power dissipation.

A dipole coil is characterized by a “midplane angle” (angular position of the first turn closest to the midplane) and a “pole angle” (angular position of the turn closest to the pole), as well as the number of layers and conductor size. The azimuthal space needed to bring out all the leads from the short correctors determines the smallest midplane angle that can be used. The shortest bending radius determines the largest pole angle that can be used. The turns that produce the most field are the ones closer to the midplane. The turns close to the pole add to the resistance, and thus power dissipation, but do not add to the dipole field proportionately. As a result, there is an optimal pole angle for a given midplane angle to achieve the same field with minimum power dissipation. As an example, Fig. 22 shows the power needed to produce 20 mT field in the 0.5 m long innermost correctors made with 4 layers of 12-gauge (approximately 2 mm x 2 mm) square copper wire. The optimal pole angle is 76.5 degrees in this case, which is shown by the filled symbol. The current needed is 16.4 A, which would require a suitable water cooling arrangement. It is envisaged that such cooling would be provided by cooling channels attached to

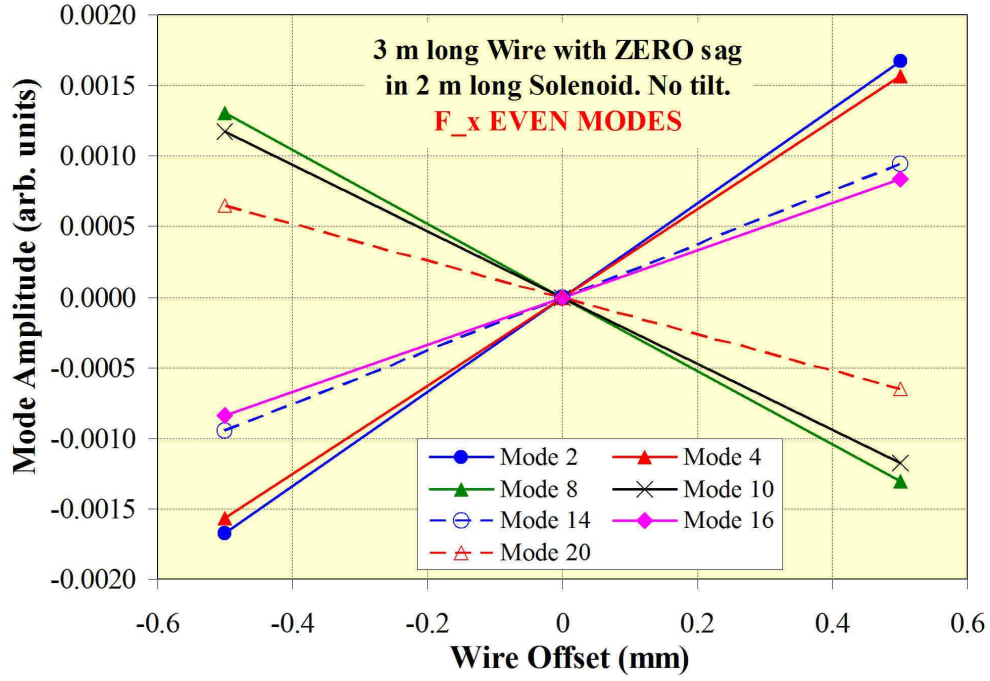


Figure 19: Amplitudes of even modes as a function of offset. The odd modes are independent of offset.

the coil support tube, as shown in Fig. 21. A similar analysis has been carried out for the other corrector layers. A summary of the optimum parameters for the two families of short correctors is given in Fig. 23. The cooling system should be capable of removing approximately 3 to 4 kW of dissipated power from each of the short corrector systems comprising of 5 correctors each. A detailed thermal analysis is needed to ensure that adequate cooling can be provided with reasonable flow rate and pressure drop, while keeping the temperature rise within acceptable limits. Furthermore, the support tubes for the coils need to be designed in such a way that there is no electrical continuity for azimuthal eddy currents to flow in the case of a quench in the solenoid.

6.3.2 Correctors for solenoid axis alignment

In addition to the local correction of the field lines, it is desirable to have full length correctors to tilt the overall solenoid axis in order to correct for any angular misalignment with the electron beam. The strength of these correctors depends on the amount of angular correction desired and the solenoid field strength. Assuming a ± 1 mrad correction range and 6 T solenoid field, the strength of the full length correctors should be 6 mT. An optimization similar to that described for the 0.5 m long correctors was carried out for these correctors also. Since the field needed is much lower as compared to the short correctors, it is sufficient to have just two layers of conductor per axis instead of four layers. The optimized parameters for the full length correctors are given in Fig. 23. The correctors for the two transverse axes share the same cooling system, which needs to remove a little over 1 kW of power in this case. As shown in Fig. 21, the warmest surface of these correctors is very close to the inner diameter of the solenoid. It may be desirable to keep the cooling channels on the outside of these correctors to minimize any risk of quenching the main solenoid. This will be addressed as part of the overall engineering design of the correction system.



Figure 20: A prototype vibrating wire system for measuring solenoids.

7 Electron collector *A. Pikin, J. Hock*

The electron collector has to dissipate the power of electron beam coming from the interaction region in the center of superconducting solenoid. The nominal current of the electron beam is 1 A and the maximum current at which the Gaussian electron gun can generate is close to 2 A with short life time. The concept of this electron collector (EC) is similar to one used in EBIS. This choice is dictated primarily by UHV requirements of RHIC, because it allows the separation of the heavily bombarded area of EC from the rest of electron lens by using a small diaphragm at the entrance into EC and a vacuum pump with good conductance at its exit. Another reason is its simple design with practically only cylindrical surfaces to be cooled. One more advantage is the optical access to its interior from the outside, which allows having optical imaging of the electron beam at the entrance into the EC for the observation of the current density profile. This collector has to be isolated from the rest of the beam pipe because its electron-bombarded surfaces are part of the vacuum enclosure and it may have voltage with respect to ground. The design of the EC is presented in Fig. 24.

To have fast diverging electron trajectories inside the EC there is a magnetic shield around its vacuum enclosure, with a small entrance diaphragm that cuts off the magnetic field inside the EC. The electron reflector has a potential lower than the cathode and pushes electrons outwards to the water-cooled cylindrical surface. There is an option of measuring the ion current from the interaction region as well. The simulated electron trajectories inside the EC are presented in Fig. 25 together with the axial distributions of the electric and magnetic fields. The axial distributions of power density in the EC are presented in Fig. 26.

The secondary electrons are not included in these simulations. Because of the redistribution of the electron beam power by secondary electrons we expect these distributions to be more uniform with somewhat less pronounced peaks and loading of surfaces which are not bombarded by primary electrons. ANSYS simulations have been done for a concentrated doubled power load from 2 A, 5 keV electron beam and for uniform power load on cylindrical surface of 50 W cm^{-2} . The results are presented in Figs. 27 and 28.

One can see that under a load twice as high as expected from a 2 A electron beam the maximum temperature on inner surface of the EC shell is 102°C . Under a uniform load of 50 W cm^{-2} it is 125°C . This temperature range is acceptable for the EC material (copper) and for UHV conditions in a RHIC beam line. In the existing EC design 20 tubes with an ID=8.0 mm are brazed to the outside of the EC cylindrical shell and are connected in parallel for water flow. The total water flow through all tubes is 20 gal/min, the pressure drop across tubes is $\Delta p = 44 \text{ kPa}$, and heat transfer coefficient is

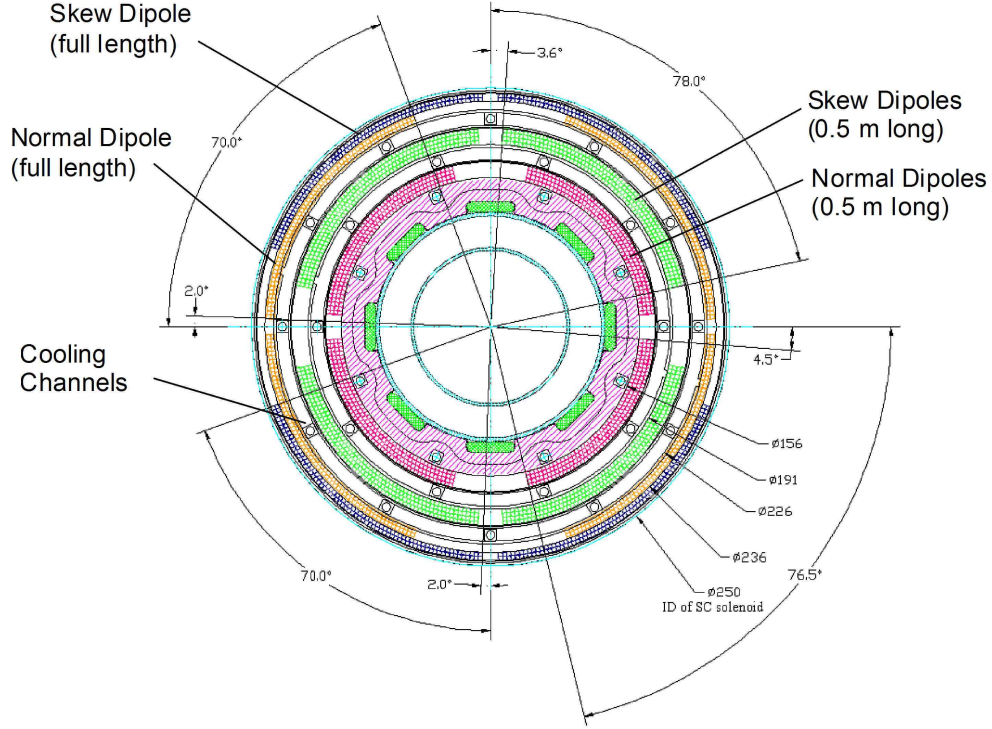


Figure 21: A cross section of the correction system showing various dipole correctors (courtesy J. Hock and A. Pikin).

$$h = 8946 \text{ W m}^{-2}\text{K}^{-1}.$$

8 Power supplies *R. Lambiase*

A block diagram of the power supplies for one electron lens is shown in Fig. 29. Most of the supplies are referenced to ground potential, but the elements in the gun end and the collector end of the device are referenced to the device cathode. A bias supply sets the voltage offset between the two potential platforms. The individual powering elements can be separated into groups.

- **Electron gun**

This includes the cathode bias supply, the cathode heater, the beam forming supply, and the two anode supplies. The anode is split into two parts, a DC element, and fast pulsed element. Splitting the anode reduces the capacitive load requirements for the fast pulsed modulator. A cathode solenoid and a focusing solenoid are powered individually in this group.

- **Electron gun to main solenoid transport**

The electron beam is transported into RHIC with three solenoids, which are powered in series, and three drift tubes, which are powered individually. There are also four sets of dipole windings, two horizontal and two vertical, to steer the beam.

- **RHIC interaction**

The superconducting solenoid has a power supply to change the current and runs in persistent mode. Within the superconducting solenoid, eight drift tubes and twenty trim magnets are powered individually. The superconducting solenoid is followed by a warm focusing solenoid.

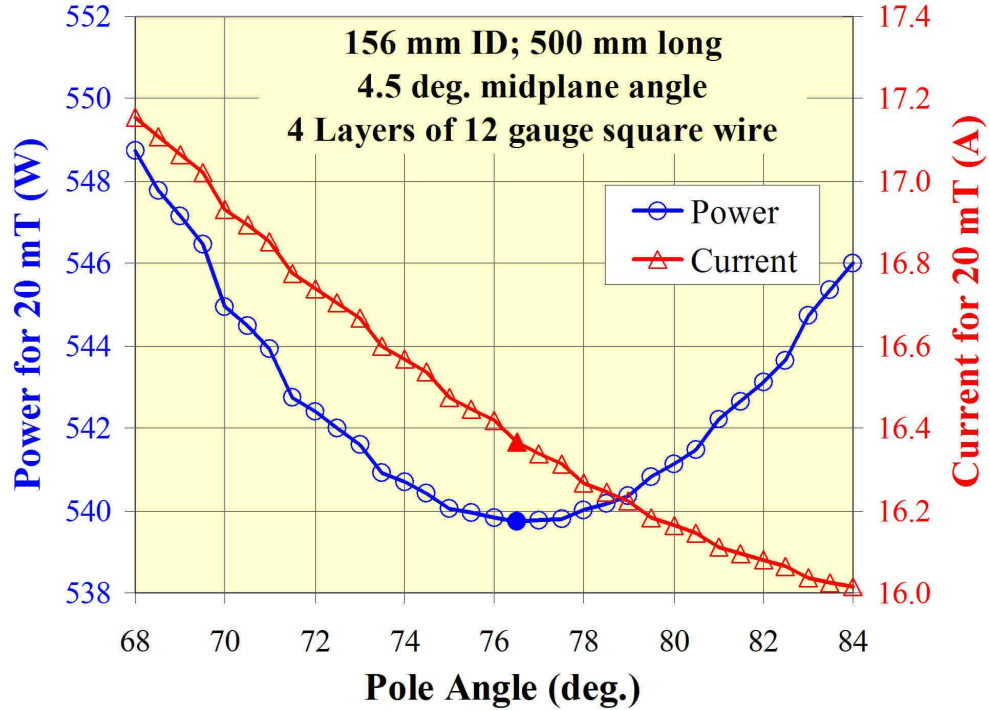


Figure 22: Power (circles) and current (triangles) needed to produce 20 mT field in a 0.5 m long corrector made using four layers of a 2 mm square copper conductor. The filled symbols represent the optimal pole angle for minimum power dissipation.

- **Main solenoid to electron collector transport**

This is identical to the transport from the electron gun to the main solenoid.

- **Electron collector**

The collector power supply is rated with 10 kV at 2 A, and will limit the energy deposited in the device should an arc occur. An ion extractor is powered with respect to the cathode potential. A suppressor element is powered with respect to the collector, so an additional isolation transformer is required.

All power supplies will be controlled with a standard BNL designed power supply interface (PSI). The PSI provides for an analog set point, four analog read backs, fifteen digital commands, and sixteen status bits. The PSI is electrically tied to the power supply it is controlling, but is electrically isolated from all other equipment, including the control system, by a pair of fiber optic cables.

9 Vacuum system *M. Mapes*

9.1 Gun and collector vacuum

The gun and collector vacuum will be required to be UHV compatible and will interface to the existing vacuum of the RHIC warm bore which is at a nominal pressure of 10^{-11} Torr. For this reason the chambers and all of the components of the gun and collector lines shall be bakable to a minimum of 250°C. All materials shall be UHV compatible metals and ceramics and no organic materials. The chamber vacuum

Parameter	Short Dipoles		Full Length Dipoles	
	Axis 1	Axis 2	Axis 1	Axis 2
Coil ID (mm)	156.0	191.0	226.0	236.0
Coil OD (mm)	174.2	209.2	235.0	245.0
No. of Layers	4	4	2	2
Midplane Angle (deg.)	4.5	3.6	2.0	2.0
Pole Angle (deg.)	76.5	78.0	70.0	70.0
Turns	191	239	125	131
Field (mT)	20.0	20.0	6.0	6.0
Current (A)	16.4	16.8	9.1	9.1
Copper Current Density (A/mm ²)	4.1	4.2	2.3	2.3
Resistance (Ohm)	2.0	2.5	6.3	6.6
Voltage (V)	33.0	42.5	57.4	60.1
Power per Corrector (W)	540	713	521	545
Power Density* (W/cm ²)	0.252	0.263	0.037	0.037
Total Power for the entire layer (W)	2699	3565	1066	

* Power Density is defined as the power per unit surface area of coil in contact with the cooling surface

Figure 23: Parameters for dipole correctors using 12-gauge (approximately 2 mm x 2 mm) square wire.

processing will include vacuum firing of all components at 450°C to reduce the bulk hydrogen in the chamber materials.

To separate the gun and collector vacuum from the solenoid magnet chamber and the RHIC warm bore there will be all-metal gate valves which will be interlocked to the pressure of the gun and collector chambers. These valves will be used to protect the RHIC warm bore vacuum should a leak or an unexpected pressure rise in either of these chambers. If the pressure trips the interlock setpoint, the valves will close isolating the gun or collector line from RHIC.

Since the gun and collector lines are very short and there is no room to add distributed pumping along each beam line large pumps are needed on the chambers to prevent pressure bumps in the RHIC warm bore where the gun and collector lines connect to the solenoid magnets. The design pressure for both the gun and collector lines will be 10^{-10} Torr.

The gun chamber gas load will be confined by using an conductance limiting aperture and high pumping speed using a combination 500 l/sec diode ion pump with supplementary NEG cartridges mounted inside the pump body. There will also be a 300 l/sec turbopump mounted with a gate valve on the gun chamber which will be used for conditioning and roughing during bakeouts.

The collector chamber will also have a conductance limiting aperture to confine the gas load of the collector being heated by a nominal heat load of 20 kW. The chamber will have two 500 l/sec diode ion pumps with dual pocket titanium sublimation pumps mounted within the pump bodies with a total pumping speed of about 2,000 l/sec.

9.2 RHIC vacuum interface

The design vacuum of the RHIC warm bore is 10^{-11} Torr. All vacuum chambers interfacing with the RHIC warm bore will be bakable to 300°C and have NEG coating deposited on the internal walls of the chambers. The activation temperature of the NEG coating will be 250°C. The NEG coating will provide linear pumping along the beamline and also suppress the effects of the electron cloud.

The two solenoid vacuum chambers will be fabricated from 6" stainless steel tubing with 8" Conflat

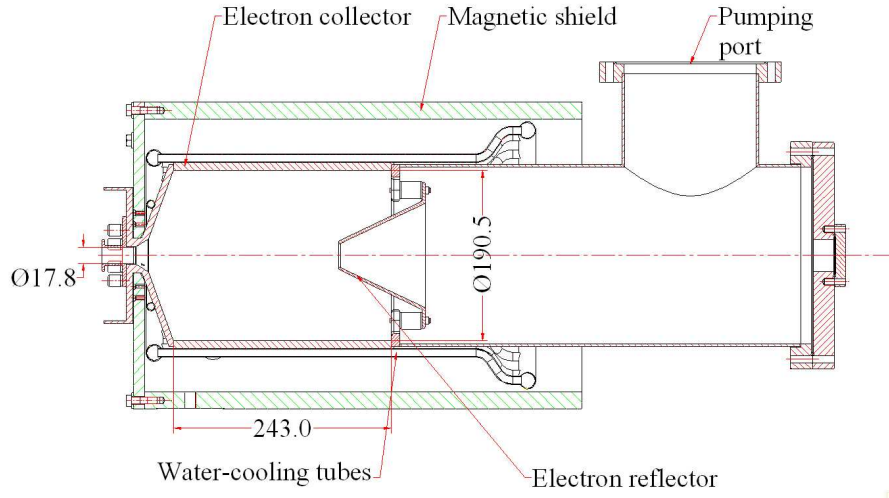


Figure 24: General design of the electron lens electron collector.

flanges. The 6" diameter tube will provide enough room to install heating jackets on the chambers and still leave room for a small air gap between the heating blankets and the wall of the solenoid magnet tube and coils.

The wye chambers connecting the solenoid chambers with the RHIC warm bore and the gun and collector lines will also be fabricated from stainless steel. These chambers will have diameter transitions which will interface the existing RHIC warm bore piping to the solenoid, gun and collector lines. All flanges used will be Conflat flanges. The vacuum processing of the chambers will include vacuum firing of all components at 450°C to reduce the bulk hydrogen in the chamber materials.

10 Instrumentation *D. Gassner, C. Montag*

The diagnostics systems plays a critical role in meeting the ambitious requirements for electron lens commissioning, set up and operation. The goal is to provide instrumentation to accurately align a small (see Tab. 1 proton beam inside a only slightly larger electron beam over the length of the electron lens solenoid, and ensure the alignment is stable for hours during the RHIC store. The relative alignment of the proton and electron beam should be about 10% of an rms beam size. This is the same beam alignment guideline used at the STAR and PHENIX experimental interaction points during the proton physics program.

RHIC set-up and study time is limited and infrequent. In order to be able to test and commission the electron lens system it is critical to run in a mode which only marginally affects the RHIC beam during physics stores. One way to achieve this is to have an electron current modulator so that the electron beam is on only during the abort gap or a few selected RHIC bunches. The instrumentation requirements for tuning are summarized in Tab. 3.

10.1 Electron current modulator

The electron gun has perveance of $0.48 \times 10^{-6} \text{ AV}^{-3/2}$ (see Fig. 30). In order to generate the electron design current (Tab. 2) of 2 A, the anode voltage will need to be 25 kV. While the electron beam is normally dc we are considering a modulator designed with Behlke switches for diagnostics. The two

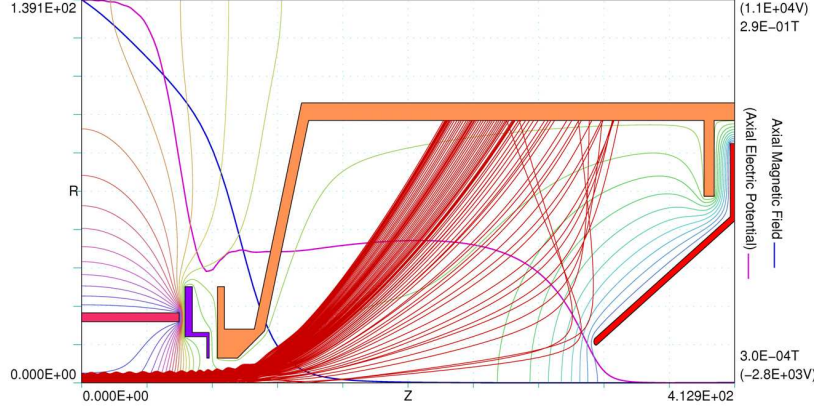


Figure 25: Simulated electron trajectories inside the collector for $I_{el} = 1.06$ A and $E_{el} = 3.0$ keV.

Table 3: RHIC electron lens instrumentation related parameters required for tuning.

parameter	expected value	accuracy	resolution	comment
electron beam position	0-10 mm	20 μm	2 μm	current modulation needed for BPMs
proton beam position	0-10 mm	20 μm	2 μm	Blue and Yellow beam in same pipe
electron beam current I_e	1-2 A	< 0.1%	< 0.01%	
proton tunes (Q_x, Q_y)	0.68	0.0001	0.0001	measurement with BTF

modes of desired modulator operation are described below:

Mode 1: parasitic setup. The electron beam is on for 1 μs (500 ns FWHM), and off for 11.7 μs . The RHIC revolution time is 12.7 μs . In this mode we can study the electron lens effect on one or several bunches after the RHIC abort gap without effecting the rest of the bunches. RHIC bunch-by-bunch diagnostics (WCM, emittance measurement with polarimeter, BTF) are critical in this mode to measure the effect that the electron lens has on the selected bunched. This pulsed electron beam will also provide a signal for the electron beam position measurement (see Fig. 31).

Mode 2: physics operations. The electron beam on for 11.7 μs and off for 1 μs to enable electron BPMs to measure the position throughout the store (see Fig. 32).

10.2 Relative electron-proton beam alignment

The relative alignment of the electron and proton beam is critical for the effectiveness of the beam-beam compensation, with alignment tolerances as low as 10% of the rms beam sizes (see Tab. 1 and Tab. 2). Although there are 3 beams sharing a common beam pipe, only relative positions of the electron beam and its respective RHIC beam is needed for optimizing the electron lens performance.

BPMs are used to bring both beams close together, while bremsstrahlung detectors and diagnostics of the proton beam and luminosity lifetime are used to maximize the overlap of the beams. The RHIC Blue and Yellow beams are vertically separated by 10 mm in IR10.

Due to the large difference in electron (1 μm) and RHIC beam bunch lengths (5 ns), separate electron and proton beam position monitors will be used. We will install two electron beam position monitors inside the e-lens solenoid. Proton beam position monitors will be installed in the RHIC warm section beam line close to the upstream end of each e-lens solenoid.

Electron BPMs. During normal electron lens operations the electron beam will be DC with < 0.1% ripple that is not detectable by typical inductive beam position monitors pick-ups. The DC beam will

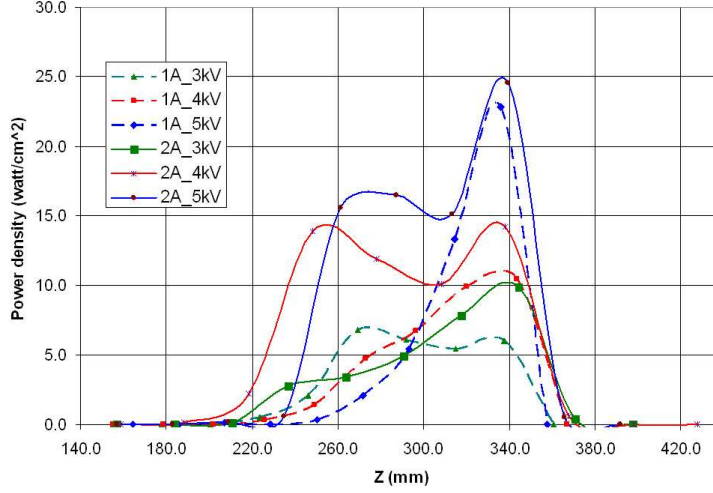


Figure 26: Axial distributions of power density in the collector for 1.06 A and 2.0 A for different electron beam energies.

be modulated on demand so the position can be accurately measured by 2 sets of dedicated strip line pick-ups inside the SC solenoid.

For the electron BPMs we are considering commercial Libera Brilliance electronics (fast digitizers with local FPGA system). Since the electron beam will be modulated by a pulse of about $1 \mu\text{s}$ long, we can frequency limit the electron beam BPMs to ignore the higher frequency proton bunches.

Proton BPMs. The existing RHIC DX BPM systems (RHIC beam parameters; f_{rf} 197MHz, 15 cm rms, 30 ps full width) at store, claim to measure individual beam positions in the common region to the $200 \mu\text{m}$ absolute, and $10 \mu\text{m}$ resolution level. Taking advantage of the beam abort gap, RHIC BPM signals can be sampled by a fast digitizer and processing in time to determine average position.

In addition to the higher resolution position requirement, we also need very low drift, and measurements that are independent of RHIC bunch patterns. A dedicated programmable triggering and delay system will need to be to synchronize the BPM electronics digitizers.

Bremsstrahlung monitor The interaction of the high energy proton beam with the electron lens results in the emission of bremsstrahlung due to the momentum transfer from the protons to the low energy electrons. Because of the non-relativistic electron beam energy, the spatial distribution of the emitted photons is almost isotropic, as Fig. 34 illustrates.

Taking advantage of this “light bulb” characteristics, two photon detectors will be installed near the ends of the electron lens, as schematically depicted in Fig. 35. This configuration allows to maximize the overlap of the proton and electron beam by eliminating relative offsets and crossing angles.

In the following, we assume a $l = 2 \text{ m}$ interaction length and detectors at a beam pipe radius of $r = 5 \text{ cm}$. Two $2 \times 2 \text{ cm}^2$ photon detectors are located in the beam pipe wall at both ends of the lens. Beam sizes and intensities are listed in Tabs. 1 and 2, case 2. In the case of a parallel offset Δr of the two beams with respect to each other, the luminosity and therefore the photon yield scales as

$$L = L_0 \cdot \exp\left(-\frac{(\Delta r)^2}{2\sigma^2}\right), \quad (16)$$

while for a crossing angle $\Delta\phi$ the luminosity contribution from each infinitesimal slice of thickness ds depends on its longitudinal position s within the electron lens. With $s_0 = 0$ being the center of the

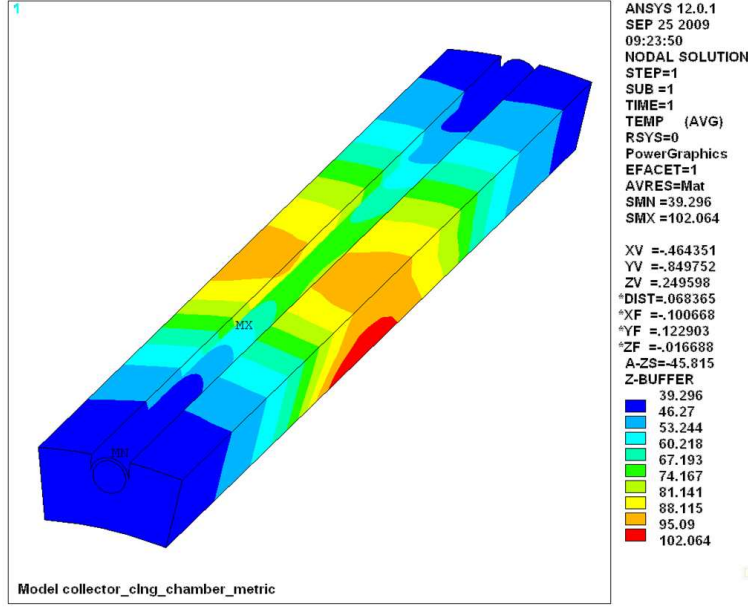


Figure 27: Temperature distribution on the collector cylindrical shell for a concentrated power load with a peak power density of 50 W cm^{-2}

electron lens, the luminosity contribution from each slice at position s is therefore

$$dL(s) = dL_0(s) \cdot \exp\left(-\frac{(\Delta r(s))^2}{2\sigma^2}\right), \quad (17)$$

with

$$\Delta r(s) = \phi \cdot s. \quad (18)$$

Using the detector arrangement depicted in Fig. 35, we can therefore calculate the photon yield in the two detectors as a function of the parallel beam offset Δr and the crossing angle ϕ , as shown in Figs. 36 and 37. Due to the non-isotropic distribution of the emitted photons, the photon yield as detected by the two detectors at the upstream and downstream end of the electron lens is slightly different. However, the functional dependence on beam offset and crossing angle is very similar.

10.3 Electron beam diagnostics

The electron beam needs to be monitored for shape and current, and current loss. The electron beam shape as a function of the gun grid settings will be measured on a test bench. It will not be measured in the completed electron lens.

Beam current monitors. Wideband commercial current transformers will be used at the gun cathode and collector to measure the electron beam current leaving the gun, and arriving at the collector (see Fig. 33). The electron beam ripple specification is $< 0.1\%$ ripple. Therefore a resolution of order 0.01% (or 0.1 mA) is needed.

The current transformer signals will be sent over long heliax cables to oscilloscopes or digitizers in the nearby service building. A commercial quality programmable Keithley current source will be used to calibrate the current transformers via a single turn calibration current path.

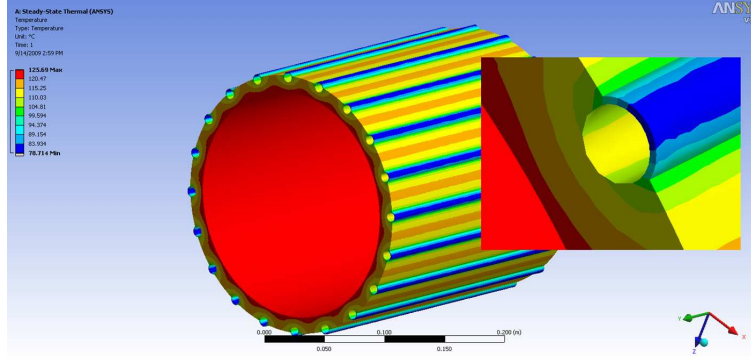


Figure 28: Simulated temperature distribution on the collector cylindrical shell under a uniform power load of 50 W cm^{-2} .

Isolated electrodes. Approximately 13 multipurpose isolated electrodes will be mounted throughout electron beam transport. The electrode detect any lost electron beam, and clear ions generated through residual gas ionization by the electron beam.

Each of these electrodes is electrically isolated from the grounded beam pipe and is wired, through vacuum feedthroughs, to coaxial cables leading out of the RHIC tunnel and to the support electronics.

10.4 Proton beam diagnostics

The proton beam is monitored with the instrumentation installed in RHIC. In addition, pin diode beam loss monitors or scintillators will be intalled as sensitive loss monitors around the electron lenses. The RHIC instrumentation needed to operate the electron lenses include

- DCCTs to monitor the beam lifetime
- WCM to monitor the bunched and bunch-by-bunch beam lifetime
- ZDC to monitor the luminosity lifetime
- IPM to monitor the average emittance
- Polarimeter to monitor the average and bunch-by-bunch emittance
- BTF to monitor the tune and tune distribution
- HF Schottky dector to monitor the tune and tune distribution

The bunch-by bunch capabilities are needed during setup when only a few bunches are affected, and to distinguish bunches that have 1 or 2 head-on collisions.

11 Infrastructure and installation *W. Fischer*

- Power needs: probably about \$1MW
- Cooling needs: probably about \$1MW
- Rack space
- Cable runs

Power and cooling is competing with the spin flipper.

12 Controls *E. Beebe, B. Oerter*

- parameters to be controlled (electron beam current, shape, position, and angle; proton beam position and angle; main solenoid field including quench protection; correction fields in solenoid; power supplies for gun, collector and drift tubes; electron beam transport solenoids and steering magnets; vacuum)
- layout of controls architecture
- required rack space, cabling, and controls hardware
- required PLC, pet, and application software

13 Commissioning and operation *W. Fischer, Y. Luo, C. Montag*

We aim for commissioning to be an activity largely parasitic to physics stores. Since the two main solenoids are of opposite polarity and close together their combined effect on linear coupling and the proton spin cancel. With this ramping the main solenoids at injection and during stores is possible, even with a ramp time of several hours to full field. A protection system must ensure that either both solenoids are on, or none.

The RHIC lattice will be prepared as to have the correct β^* -values at IP6, IP8, and IP10 (see Tab. 1), and phase advances close to a multiple of π between IP8 and IP10 in both transverse planes. The transverse phase shifter allows to adjust the vertical phases between IP8 and IP10.

Initial alignment of the electron and proton beams can be achieved with an electron beam that is only active during the abort gap. Commissioning of the electron lens can then proceed with a large electron beam size and low electron current. Under these conditions the electron and proton beams can be aligned with further using the bremsstrahlungs monitors. When alignment is optimized, the electron beam size can be decreased by increasing the main solenoid field, and the electron beam current can be increased. During the optimization process the proton beam lifetime is monitored, and the tune distribution with transverse beam transfer functions.

In operation, the proton beam-electron lens collision should be similar to the beam-beam collisions in IP6 and IP8. These can be well reproduced when the orbits are under control. To go into collision, transverse separation bumps are removed in IR6 and IR8. Transverse bumps can also be used in IR10 to bring the proton beam into collision with the electron beam at the same time.

14 Acknowledgements

We are thankful for discussion and support to many, in particular N. Abreu (PSI), J. Alessi (BNL), G. Ganetis (BNL), E. Haug (University of Tübingen), W. Herr (CERN), A. Kabel (SLAC), H.-J. Kim (FNAL), V. Kamedzhiev (FNAL), J.-P. Koutchouk (CERN), E. McIntosh (CERN), K. Mirabella (BNL), W. Nakel (University of Tübingen), K. Ohmi (KEK), T. Pieloni (CERN), J. Qing (LBNL), T. Roser (BNL), F. Schmidt (CERN), T. Sen (FNAL), L. Snydstrup (BNL), V. Shiltsev (FNAL), G. Sterbini (CERN), A. Valishev (FNAL), and F. Zimmermann (CERN).

References

- [1] W. Fischer, M. Blaskiewicz, J.M. Brennan, P. Cameron, R. Connolly, C. Montag, S. Peggs, F. Pilat, V. Ptitsyn, S. Tepikian, D. Trbojevic, and J. van Zeijts, proceedings PAC'03, pp. 135-137 (2003).
- [2] V. Ptitsyn et al., proceedings EPAC'06, pp. 592-594 (2006).

- [3] C. Montag, PAC09 [fill in details].
- [4] E. Keil, proceedings PAC'89, pp. 1731-1735 (1989).
- [5] Y. Alexahin, proceedings PAC'05, pp. 544-548 (2005).
- [6] M. Anerella et al., Nucl. Instrum. Methods A **499**, pp. 280-315 (2003).
- [7] <http://www.fieldp.com/>
- [8] G. Kuznetsov, Nucl. Instrum. Methods A **340**, pp. 204-208 (1994).
- [9] J.-P. Koutchouk, in CERN-2009-004 (2009); CARE-Conf-08-032-HHH (2008).
- [10] L.R. Evans and J. Gareyte, proceedings PAC'83, pp. 2397-2399 (1983).
- [11] L. Evans, J. Gareyte, M. Meddahi, R. Schmidt, proceedings PAC'89, pp. 1403-1405 (1989).
- [12] K. Cornelis, M. Meddahi, R. Schmidt, proceedings EPAC'90, pp. 1670-1672 (1990).
- [13] K. Cornelis, proceedings LHC'99, CERN-SL-99-039 AP (1999).
- [14] X. Zhang, T. Sen, V. Shiltsev, M. Xiao, Y. Alexahin, F. Schmidt, F. Zimmermann, proceedings PAC'03, pp. 1757-1759 (2003).
- [15] V. Shiltsev, Y. Alexahin, V. Lebedev, P. Lebrun, R. S. Moore, T. Sen, A. Tollestrup, A. Valishev, and X. L. Zhang, Phys. Rev. ST Accel. Beams 8, 101001 (2005).
- [16] A. Valishev, proceedings EPAC'08, pp. 2937-2941 (2008).
- [17] W. Herr, proceedings PAC'91, pp. 1068-1070 (1991).
- [18] J. Gareyte, proceedings LHC'99, CERN-SL-99-039 AP, pp. 28-32 (1999).
- [19] L.H.A. Leunissen, H. Grote, and F. Schmidt, proceedings EPAC'00, pp. 1208-1210 (2000).
- [20] M.P. Zorzano and F. Zimmermann, proceedings EPAC'00, pp. 1229-1231 (2000).
- [21] O. Brüning, P. Collier, P. Lebrun, S. Myers, R. Ostojic, J. Poole, P. Proudlock (editors), CERN-2004-003 (2004).
- [22] F. Zimmermann, proceedings PAC'07, pp. 714-718 (2007).
- [23] J.-P. Koutchouk, proceedings PAC'07, pp. 3387-3389 (2007).
- [24] U. Dorda, PhD thesis, Vienna University of Technology, Austria (2008).
- [25] T. Pieloni, PhD thesis, Ecole Polytechnique Federale de Lausanne, Switzerland (2008).
- [26] W. Fischer, Y. Luo, N. Abreu, R. Calaga, C. Montag, G. Robert-Demolaize, U. Dorda, J.-P. Koutchouk, G. Sterbini, F. Zimmermann, H.-J. Kim, T. Sen, V. Shiltsev, A. Valishev, J. Qiang, and A. Kabel, in CERN-2009-004 (2009); CARE-Conf-08-032-HHH (2008).
- [27] S. Peggs, in "Handbook of accelerator physics and engineering", 3rd printing, World Scientific, pp. 166 (2006)
- [28] J.E. Augustin et al., Vol. 2, proceedings HEACC'69 (1969).
- [29] G. Arzelia et al., Proc. 8th Int. Conf. High Energy Acc., pp. 150 (1971).
- [30] Y. Ohnishi and K. Ohmi, in AIP Conference Proceedings 693 (2003)
- [31] M. Bergher et al., proceedings PAC'79, pp. 3559-3561 (1979).
- [32] H. Zygner, AIP Conference Proceedings **57**, p. 136 (1979).

- [33] Ya.S. Derbenev, proceedings 3rd All-Union Conference on Accelerators, Moscow (1972); INP 70-72 (1972); SLAC TRANS 151 (1973).
- [34] E. Keil, proceedings of the 3rd ICFA Beam Dynamics Workshop; CERN-LEP-TH/89-37 (1989).
- [35] B. Podobedov and R.H. Siemann, Phys. Rev. E 52, 3066 (1995).
- [36] R. Talman, private communication (1976).
- [37] E. Tsyganov, R. Meinke, W. Nexsen, A. Zinchenko, SSCL-PREPRINT-519 (1993).
- [38] E. Tsyganov, E. Tarantin, A. Zinchenko, JINR-E9-96-4 (1996).
- [39] V. Shiltsev, V. Danilov, D. Finley, and A. Sery, Phys. Rev. ST Accel. Beams 2, 071001 (1999).
- [40] E.N. Tsyganov, A. Tarantin, and A.I. Zinchenko, CERN SL-Note-95-116-AP (1995).
- [41] E. Tsyganov, A. Taragin, and A. Zinchenko, JINR-E9-96-4 (1996).
- [42] W. Fischer, O. Brüning, J.-P. Koutchouk, F. Zimmermann, T. Sen, V. Shiltsev, K. Ohmi, M. Furman, Y. Cai, and A. Chao, BNL C-A/AP/291; ICFA Beam Dynamics Newsletter No. 44, pp. 220-225; proceedings of BEAM'07, CERN-2008-005, CARE-Conf-08-004-HHH (2008).
- [43] E. Keil, CERN 95-06, pp. 539-555 (1995).
- [44] D.A. Edwards and M. Syphers, in "Handbook of accelerator physics and engineering", 3rd printing, World Scientific, pp. 65 (2006)
- [45] V. Shiltsev et al., Phys. Rev. ST Accel. Beams 11, 103501 (2008).
- [46] X.-L. Zhang, K. Bishofberger, V. Kamerdzhev, V. Lebedev, V. Shiltsev, R. Thurman-Keup, and A. Tollestrup, Phys. Rev. ST Accel. Beams 11, 051002 (2008).
- [47] V. Shiltsev, Y. Alexahin, K. Bishofberger, V. Kamerdzhev, G. Kuznetsov, and X.-L. Zhang, Phys. Rev. Lett. 99, 244801 (2007).
- [48] Y. Luo and W. Fischer, BNL C-A/AP/286 (2007).
- [49] W. Fischer, O. Brning, J.-P. Koutchouk, F. Zimmermann, T. Sen, V. Shiltsev, K. Ohmi, M. Furman, Y. Cai, and A. Chao, BNL C-A/AP/291; ICFA Beam Dynamics Newsletter No. 44, pp. 220-225; proceedings of BEAM'07, CERN-2008-005, CARE-Conf-08-004-HHH (2008).
- [50] Y. Luo, W. Fischer, and N. Abreu, BNL C-A/AP/310 (2008).
- [51] Y. Luo, W. Fischer, N. Abreu, E. Beebe, J. Beebe-Wang, C. Montag, M. Okamura, A. Pikin, and G. Robert-Demolaize, proceeding EPAC'08 (2008).
- [52] N.P. Abreu, W. Fischer, Y. Luo, and G. Robert-Demolaize, proceeding EPAC'08 (2008).
- [53] Y. Luo, G. Robert-Demolaize, N. Abreu, and W. Fischer, proceeding EPAC'08 (2008).
- [54] N.P. Abreu, W. Fischer, Y. Luo, G. Robert-Demolaize, BNL C-A/AP/346 (2009).
- [55] N.P. Abreu, W. Fischer, Y. Luo, G. Robert-Demolaize, BNL C-A/AP/347 (2009).
- [56] Y. Luo, N.P. Abreu, R. de Maria, W. Fischer, G. Robert-Demolaize, and E. McIntosh, proceedings PAC'09 (2009).
- [57] A. Valishev, Y. Luo, and W. Fischer, BNL C-A/AP/353 (2009).
- [58] W. Fischer, N.P. Abreu, R. Calaga, R. de Maria, Y. Luo, C. Montag, G. Robert-Demolaize, T. Sen, and H.J. Kim, proceedings PAC'09 (2009).
- [59] See, for example, http://www.group3technology.com/group3_meters.php
- [60] Data sheet at http://www.senis.ch/images/x-HYx-xx_EYD-2.5kHz-0.1-10T.pdf

- [61] C. Crawford, et al., Proc. PAC99, New York, pp. 3321-3 (1999).
- [62] C. Crawford, et al., Proc. PAC 2001, Chicago, pp. 195-7 (2001).
- [63] A. Temnykh, Nucl. Instrum. Methods A **399** pp. 185-194 (1997).
- [64] A. Jain, et al., Proc. the 10th International Workshop on Accelerator Alignment, KEK, Tsukuba, 11-15 February 2008, available at: <http://www.slac.stanford.edu/econf/C0802113/papers/P019.pdf> (2008).

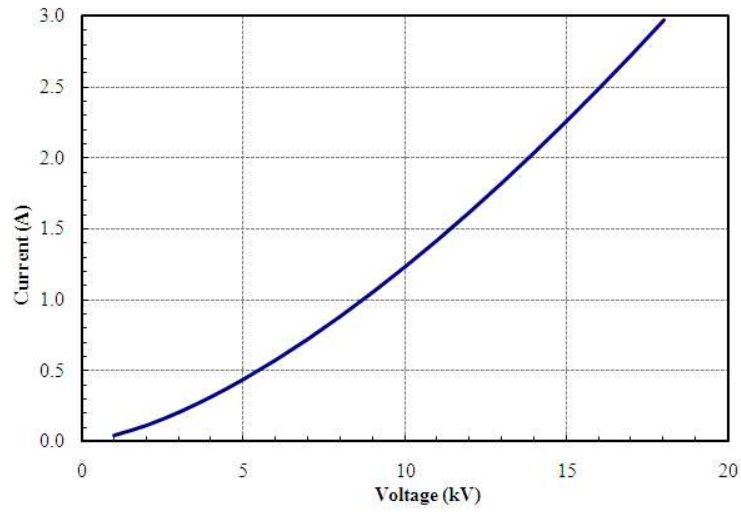


Figure 30: Electron gun current as a function of the anode voltage for a perveance of $1.23 \mu\text{AV}^{-3/2}$.

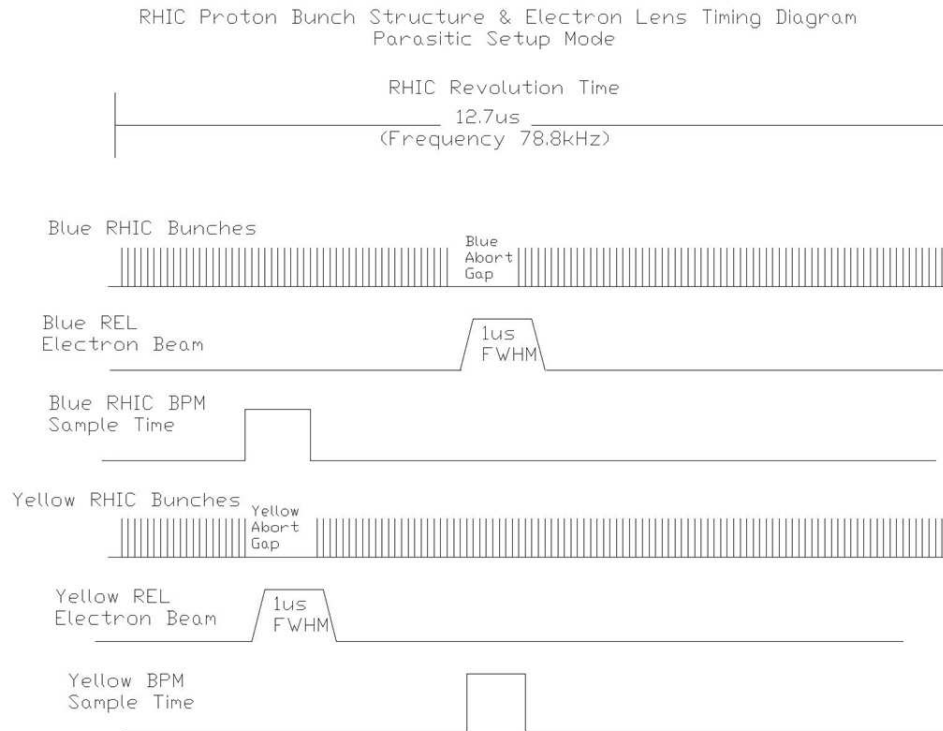


Figure 31: Parasitic setup mode.

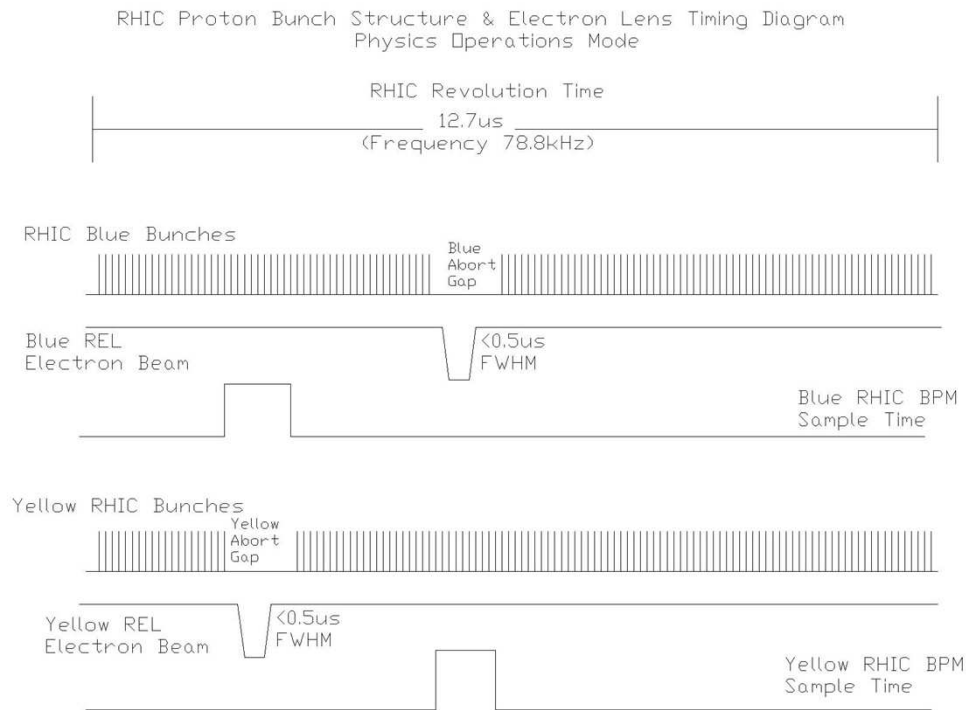


Figure 32: Operations mode.

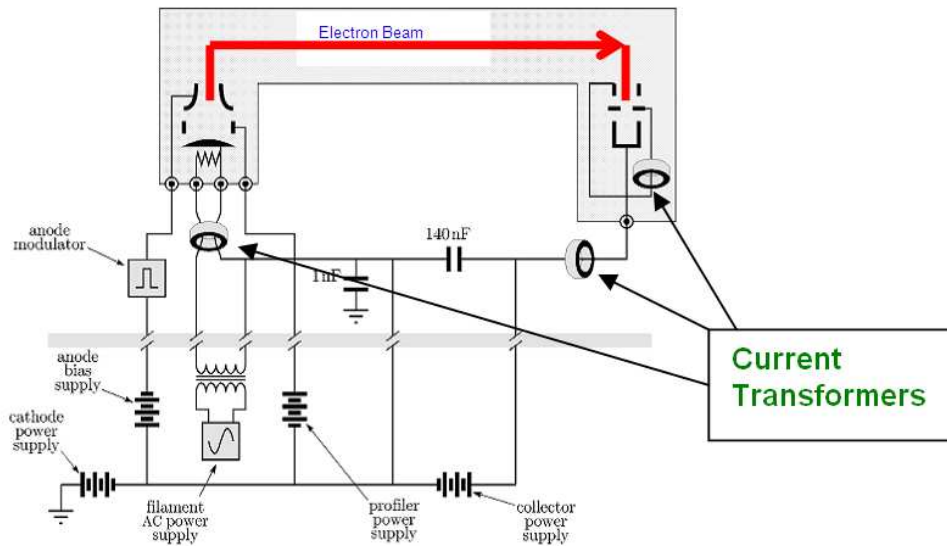


Figure 33: Electron current monitors (V. Shiltsev FNAL TEL NJP 2008).

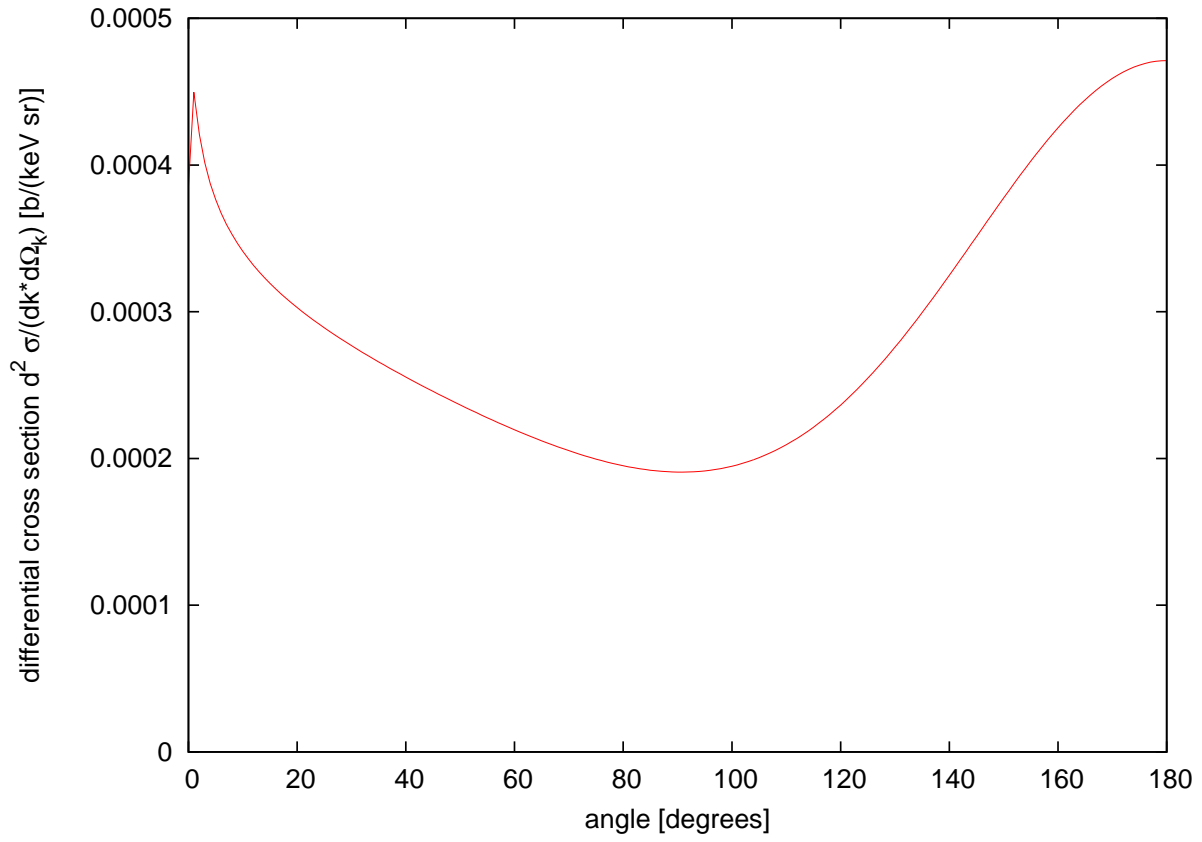


Figure 34: Differential cross section $d^2\sigma/(dk \cdot d\Omega_k)$, for $E_p = 250$ GeV, $E_e = 10$ keV, and a photon energy of $k = 10$ keV. Zero degrees corresponds to the direction of the proton beam.

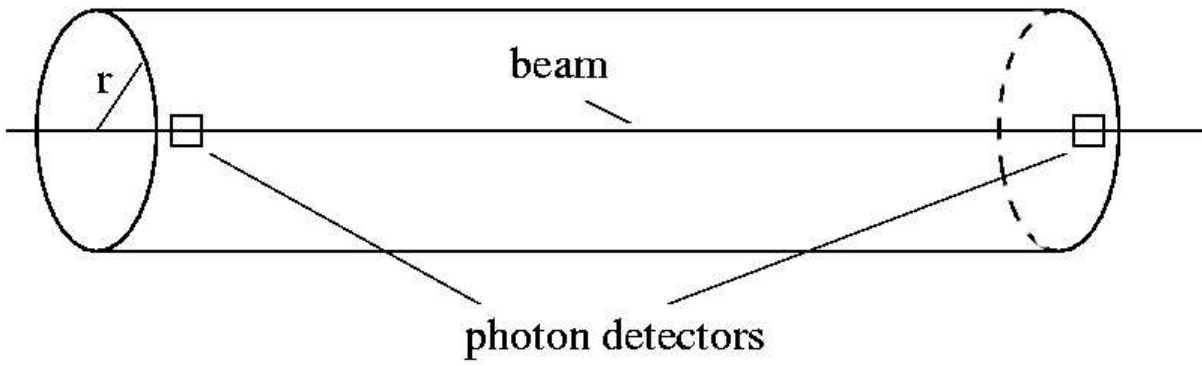


Figure 35: Photon detector configuration

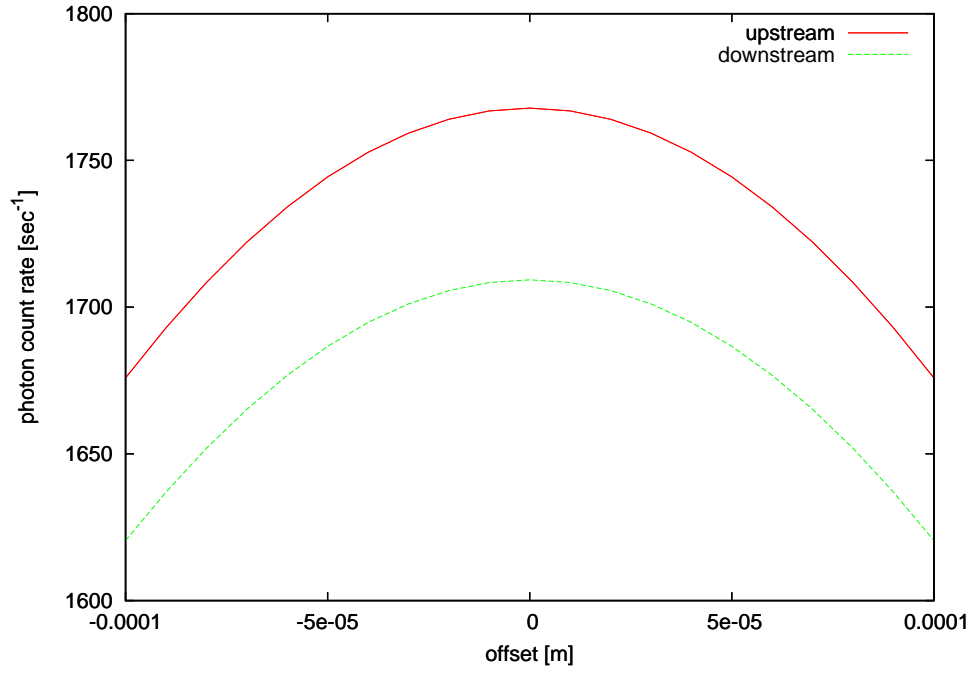


Figure 36: Photon rate as function of offset Δr at the two photon detectors.

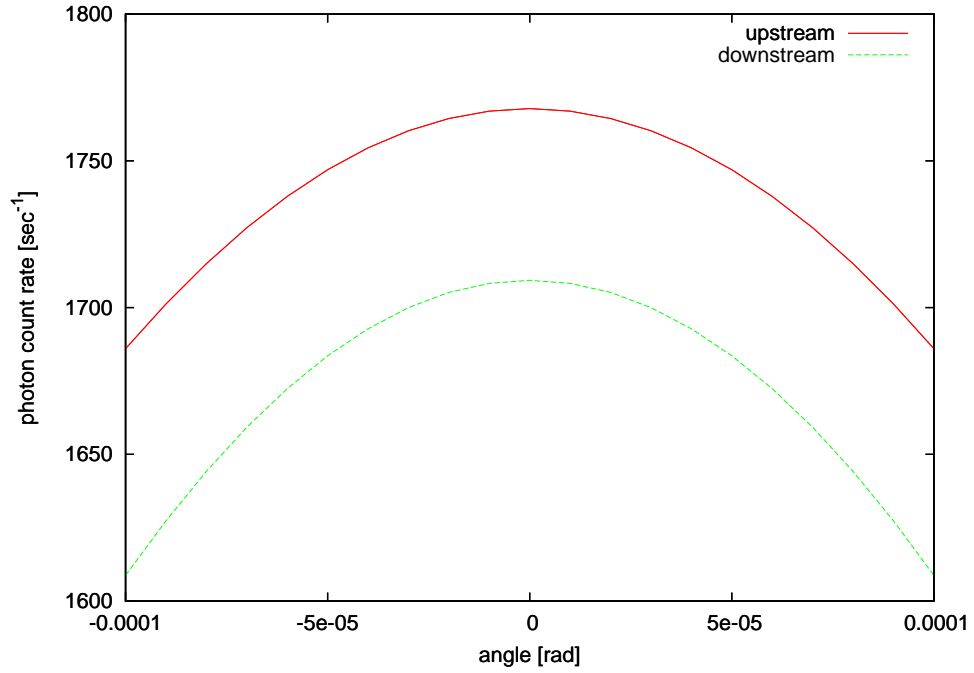


Figure 37: Photon rate as function of crossing angle ϕ at the two photon detectors.